Bispecific aptamer-decorated and light-triggered nanoparticles targeting tumor and stromal cells in breast cancer derived organoids: implications for precision phototherapies

Simona Camorani
Istituto per l'endocrinologia e l'oncologia Gaetano Salvatore
Alessandra Caliendo
Istituto per l'endocrinologia e l'oncologia Gaetano Salvatore
Elena Morrone
CNR NANOTEC: Istituto di Nanotecnologia Consiglio Nazionale delle Ricerche
Lisa Agnello
Istituto per l'endocrinologia e l'oncologia Gaetano Salvatore
Matteo Martini
University of Lyon 1: Universite Claude Bernard Lyon 1
Monica Cantile
Istituto Nazionale Tumori IRCCS Fondazione Pascale
Margherita Cerrone
Istituto Nazionale Tumori IRCCS Fondazione Pascale
Antonella Zannetti
Istituto di Biostrutture e Bioimmagini Consiglio Nazionale delle Ricerche
Massimo La Deda
Università della Calabria: Universita della Calabria
Monica Fedele
Istituto per l'endocrinologia e l'oncologia Gaetano Salvatore
Loredana Ricciardi
CNR NANOTEC: Istituto di Nanotecnologia Consiglio Nazionale delle Ricerche
Laura Cerchia
cerchia@unina.it

Istituto per l'Endocrinologia e l'Oncologia Sperimentale (IEOS) del Consiglio Nazionale delle Ricerche
https://orcid.org/0000-0002-7633-7932

Research Article

Keywords: Aptamer, EGFR, PDGFRβ, Dual targeting, Nanomedicine, Patient-derived cancer organoids, Phototherapy, Tumor microenvironment

Posted Date: February 6th, 2024

DOI: https://doi.org/10.21203/rs.3.rs-3917820/v1

Version of Record: A version of this preprint was published at Journal of Experimental & Clinical Cancer Research on March 26th, 2024. See the published version at https://doi.org/10.1186/s13046-024-03014-x.

Abstract

Background

Based on the established role of cancer-stroma cross-talk in tumor growth, progression and chemoresistance, targeting interactions between tumor cells and their stroma provides new therapeutic approaches. Dual-targeted nanotherapeutics selectively acting on both tumor and stromal cells may overcome the limits of tumor cell-targeting single-ligand nanomedicine due to the complexity of the tumor microenvironment.

Methods

Gold-core/silica-shell nanoparticles embedding a water-soluble iridium(III) complex as photosensitizer and luminescent probe (Ir_{en}-$AuSiO_2$_COOH) were efficiently decorated with amino-terminated EGFR (CL4) and PDGFRβ (Gint4.T) aptamers (Ir_{en}-$AuSiO_2$_Aptamer). The targeting specificity, and the synergistic photodynamic and photothermal effects of either single- and dual-aptamer-decorated nanoparticles have been assessed by confocal microscopy and cell viability assays, respectively, on different human cell types including mesenchymal subtype triple-negative breast cancer (MES-TNBC) MDA-MB-231 and BT-549 cell lines (both EGFR and PDGFRβ positive), luminal/HER2-positive breast cancer BT-474 and epidermoid carcinoma A431 cells (only EGFR positive) and adipose-derived mesenchymal stromal/stem cells (MSCs) (only PDGFRβ positive). Cells lacking expression of both receptors were used as negative controls. To take into account the tumor-stroma interplay, fluorescence imaging and cytotoxicity were evaluated in preclinical three-dimensional (3D) stroma-rich breast cancer models.

Results

We show efficient capability of Ir_{en}-$AuSiO_2$_Aptamer nanoplatforms to selectively enter into target cells, and kill them, through EGFR and/or PDGFRβ recognition. Importantly, by targeting $EGFR^+$ tumor/$PDGFR\beta^+$ stromal cells in the entire tumor bulk, the dual-aptamer-engineered nanoparticles resulted more effective than unconjugated or single-aptamer-conjugated nanoparticles in either 3D spheroids cocultures of tumor cells and MSCs, and in breast cancer organoids derived from pathologically and molecularly well-characterized tumors.

Conclusions

Our study proposes smart, novel and safe multifunctional nanoplatforms simultaneously addressing cancer-stroma within the tumor microenvironment, which are: (i) actively delivered to the targeted cells through highly specific aptamers; (ii) localized by means of their luminescence, and (iii) activated via minimally invasive light, launching efficient tumor death, thus providing innovative precision therapeutics.

Given the unique features, the proposed dual targeted nanoformulations may open a new door to precision cancer treatment.

Background

Diverse components of the breast cancer microenvironment, including fibroblasts, mesenchymal stem cells, macrophages, adipocytes and altered extracellular matrix, synergistically promote tumor growth, invasion and metastasis, and resistance to therapy [1]. A continuous remodeling of the architecture of the tumor occurs in response to the dynamic signaling between tumor cells and stromal cells [2]. These stromal cells are actively recruited from the other tissues to the tumor site, where they shift from a neutral or anti-tumor behavior toward a pro-tumorigenic role [3]. Mesenchymal stem/stromal cells "educated" by tumor cells promote malignant features including proliferation, epithelial-mesenchymal transition, propagation of cancer stem cells, angiogenesis, inhibition of apoptosis, immune system suppression, evasion of immune surveillance and drug resistance [4]. Therefore, in the search for new effective anticancer therapies, it is mandatory to take into account the complex cross-talk between cancer cells and neighboring stromal cells. In this context, procedures for developing three-dimensional (3D) stroma-rich coculture models are increasing fast as they enable investigations related to intercellular dialogue within the tumor microenvironment (TME). Multicellular tumor spheroids, consisting of tumor and stromal cells, and patient-derived cancer organoids (PDCOs) recapitulating in vitro the complex structure and function of the original cancer, are more accessible than a living system in a variety of biological studies [5–7] and are essential for cancer research and drug development [8].

The rapid development of nanomaterials has led to remarkable advances in the field of cancer treatment [9]. Among them, light-responsive nanomaterials have received a great deal of attention for application in phototherapy, i.e. Photodynamic Therapy (PDT) and Photothermal Therapy (PTT) [10–12]. In PDT, photosensitizers absorb and transfer light energy to surrounding molecules, generating cytotoxic reactive oxygen species, resulting in the activation of apoptotic processes; in particular, nanomaterials are used in PDT as carriers or as active agents [13, 14]. In PTT, photothermal conversion agents are able to capture light energy and convert it into heat, triggering cancer cell death by temperature-dependent necrosis [15]. Among all, noble-metal-based nanoparticles, due to their thermoplasmonic properties, proved to be efficient nano-sources of heat for PTT application [16]. Both treatment approaches, as well as to the possibility of being used in combination to develop synergistic effects [15], ensure a high spatio-temporal control of the cytotoxic activity in the limited area exposed to irradiation, thus limiting systemic side effects. In this frame, we have previously reported the synthesis and characterization of a multifunctional nanoplatform for combined PDT and PTT treatments, based on a gold-core and silica-shell structure, embedding in the polysiloxane matrix an iridium(III) compound ($[Ir(ppy)_2(en)]OOCCH_3$, where ppy = 2-phenylpyridine and en = ethylenediamine, Ir_{en}), employed as photosensitizer and luminescent probe [17, 18].

Here, we succeeded in preparing a multifunctional nanosystem having two different RNA aptamers conjugated on the external surface of Ir_{en}-embedded gold-core/silica-shell-based nanoparticles for synergistic PDT and PTT on either 3D cocultures of tumor cells and stromal cells, and breast cancer derived

organoids. Specifically, for tumor cell targeting we used the CL4 2'Fluoro-pyrimidines (2'F-Py) RNA aptamer (Kd, 10 nM; 39 nt) [19], capable of binding at high efficacy to the extracellular domain of epidermal growth factor receptor (EGFR), one of the most potent oncoprotein of human cancer. The aptamer has excellent capability to recognize EGFR-positive cells belonging to different cancer types [19, 20], including human epidermal growth factor receptor 2 (HER2)-positive tumors [21, 22] and triple-negative breast cancer (TNBC) [23]. Moreover, due to its selectivity, CL4 has been extensively used by our group [24] and others [25–29] to decorate different kinds of drug-loaded nanoformulations to target breast cancers implanted in mice.

On the other hand, for stromal cells targeting we used the 2'F-Py RNA Gint4.T aptamer (Kd, 9.6 nM; 33 nt) [20], which binds to the extracellular domain of platelet-derived growth factor receptor β (PDGFRβ), an established marker of stromal cells, including mesenchymal stem cells [30], cancer associated fibroblasts [31, 32], tumor-associated endothelial cells [33], immune cells [34, 35], and macrophages [36–38]. Our previous studies showed the ability of Gint4.T to bind to/inhibit PDGFRβ that is expressed on the surface of TNBC cells of the highly malignant and invasive mesenchymal subtype (MES) [39], accordingly to their undifferentiated and mesenchymal phenotype. Importantly, the aptamer binds to different TME components, including mesenchymal stem cells [30], T cells [35] and endothelial cells of vessels that vascularize the tumor [40], thus ultimately hampering their pro-tumorigenic function.

Our results show for the first time the striking potential of the dual EGFR and PDGFRβ aptamer-functionalized nanosystems for simultaneous targeting and photo-induced killing of breast tumor cells and stromal cells within the TME. The proposed strategy will represent a significant advance in nanomedicine, as it can be adapted to treat other tumors as well.

Methods

Chemicals and aptamers

4-(1,1,3,3-Tetramethylbutyl)phenyl-polyethylene glycol (Triton X-100), n-hexanol, cyclohexane, ammonium hydroxide solution (28% w/w), hydrogen tetrachloroaurate (III) trihydrate ($HAuCl_4 \cdot 3H_2O$), sodium 2-mercaptoethanesulfonate (Mesna), sodium borohydride ($NaBH_4$), (3-aminopropyl)triethoxysilane (APTES), tetraethoxysilane (TEOS), N-(3-dimethylaminopropyl)-N'-ethylcarbodiimide hydrochloride (EDC), N-hydroxysuccinimide (NHS) and phosphate buffer saline tablets were purchased from Sigma-Aldrich (Saint Louis, MO, USA). 11-Triethoxysilylundecanoic acid (95%) and N-(3-triethoxysilyl) propylsuccinic anhydride (94%) were purchased from ABCR (Karlsruhe, Germany). Ultrapure water (Milli-Q, 18 MΩ·cm) was used for the preparation of the aqueous solutions and for all rinses. Phosphate buffer solution (PBS, pH 7.4) was prepared by dissolving one phosphate buffer saline table in 200 mL of Milli-Q water. All other solvents used were of analytical grade.

NH_2-terminated 2'F-Py-containing RNA, CL4, its scrambled sequence (Scr) used as a negative control, and Gint4.T were synthesized by LGC Biosearch Technologies (Risskov-Denmark).

The sequences are as follows:

CL4: 5' (NH_2-C6)GCCUUAGUAACGUGCUUUGAUGUCGAUUCGACAGGAGGC 3'

Scr: 5' (NH_2-C6)UUCGUACCGGGUAGGUUGGCUUGCACAUAGAACGUGUCA 3'

Gint4.T: 5' (NH_2-C6)UGUCGUGGGGCAUCGAGUAAAUGCAAUUCGACA 3'

Synthesis of nanoparticles

Multifunctional gold-core/silica-shell nanoparticles embedding the photosensitizing and luminescent molecule Ir_{en} [41] were synthesized following a previously reported protocol [17, 18] with slight modifications. Briefly, quaternary water/oil (W/O) microemulsion was prepared by mixing 3.6 mL of Triton X-100, 3.6 mL of n-hexanol, 15 mL of cyclohexane and a water solution consisting of 0.9 mL $HAuCl_4 \cdot 3H_2O$ (12.75 mM), 0.9 mL Mesna (36.5 mM) and 0.3 mL $NaBH_4$ (423 mM). Then, Ir_{en} (7 mg/0.1 mL water) was added to the microemulsion, followed by the addition of 0.010 mL of APTES and 0.150 mL of TEOS. After 30 min, 0.080 mL of ammonium hydroxide solution was added. The mixture was stirred overnight at room temperature (RT). Afterward, the functionalization of the nanoparticle surface with carboxyl-terminated aliphatic chains, was carried out by addition after 24, 24 + 3 and 48 h of 0.015 mL of 11-Triethoxysilylundecanoic acid. Finally, in order to improve the colloidal stability, the silane coupling agent N-(3-triethoxysilyl) propylsuccinic anhydride (0.015 mL) was added after 48 + 3 h. The mixture was stirred overnight at RT. Then, the microemulsion was broken by addition of isopropanol and water in a volume ratio 1:1:1. Purification steps by centrifugal ultrafiltration (Vivaspin 20 PES, 100,000 MWCO, Sartorius, Gottingen, Germany) allowed the complete removal of all unreacted species. The obtained nanoparticles (Ir_{en}-$AuSiO_2$_COOH) were finally dispersed in water to a final volume of 20 mL and filtered by a 200 nm nylon membrane (Sartorius).

Ir_{en}-$AuSiO_2$_COOH were conjugated with the selected aptamers through a covalent bond between the carboxyl group (– COOH) of the nanoparticle surface coating agent and the amino group (– NH_2) on the 5'-end of RNA scaffold.

Before each treatment, the aptamers were subjected to a short denaturation-renaturation step (85°C for 5 min, ice for 3 min, 37°C for 10 min) to facilitate their folding into the minimum energy structures, which is responsible for specific binding. 1 mL of EDC (26 mM) was mixed under stirring to 1 mL of Ir_{en}-$AuSiO_2$_COOH nanoparticles solution. Then, 1 mL of NHS (24.3 mM) was added to the reaction solution. After 50 min, 3 mL of PBS were added, followed by the addition of 1 mL of an aqueous solution of CL4 (0.280 μM), Scr (0.280 μM) and Gint4.T (0.280 μM), respectively, and of 0.5 mL of CL4 (0.280 μM) and 0.5 mL of Gint4.T (0.280 μM) to get the dual aptamer-decorated preparation. The reaction continued for 24 h. Afterward, aptamer-nanoconjugates Ir_{en}-$AuSiO_2$_CL4, Ir_{en}-$AuSiO_2$_Scr, Ir_{en}-$AuSiO_2$_Gint4.T and Ir_{en}-$AuSiO_2$_CL4_Gint4.T were washed by centrifugal filter devices (Vivaspin 20 PES, 100,000 MWCO, Sartorius) to eliminate unconjugated aptamers and unbound reaction components, and concentrated to a final volume

of 1 mL, then stored at 4°C until use. The same procedure, without aptamers addition, was followed to obtain Ir_{en}-$AuSiO_2$_COOH/NHS nanoparticles in order to use them as control.

Characterization of nanoparticles

The synthesized Ir_{en}-$AuSiO_2$_COOH nanoparticles were characterized by Transmission Electron Microscopy (TEM), Dynamic Light Scattering (DLS) and UV-Vis spectroscopy.

The morphology was observed using a JEOL 2010F transmission electron microscope. The sample was prepared by depositing a drop of a diluted colloidal solution on 200 mesh carbon-coated copper grids. After evaporation of the solvent in air at RT, the nanoparticles were observed at an operating voltage of 80 kV. The hydrodynamic sizes and ζ-potential values were measured with a Zetasizer Nano ZS (Malvern) instrument (632.8 nm, 4 mW HeNe gas laser, avalanche photodiode detector, 173° detection), using glass cuvettes (1 x 1 cm) and disposable folded capillary zeta cells, respectively, and the results expressed as average of three measurements. Extinction and excitation/emission spectra were recorded with a PerkinElmer Lambda 900 spectrophotometer and Perkin-Elmer LS-50B spectrofluorometer, using quartz cuvettes with a light path 1 x 0.4 cm. The calculation of the nanoparticles concentration (number of nanoparticles per mL) and the yield of encapsulation of Ir_{en} (number of Ir_{en} molecules per nanoparticle) were carried out according to the procedure previously reported [42]. Absorption spectra were acquired over time (over one month) to monitor the stability of the nanostructures in the aqueous medium.

To validate the presence of the target-specific aptamers on the nanoparticles surface, Ir_{en}-$AuSiO_2$_CL4, Ir_{en}-$AuSiO_2$_Scr, Ir_{en}-$AuSiO_2$_Gint4.T and Ir_{en}-$AuSiO_2$_CL4_Gint4.T were characterized by DLS and UV-Vis spectroscopy techniques.

Reverse transcription-quantitative polymerase chain reaction (RT-qPCR) based assay was performed to determine the amount of aptamer conjugated to the nanoparticles as previously described [40]. Briefly, 0.1 mL of Ir_{en}-$AuSiO_2$_CL4, Ir_{en}-$AuSiO_2$_Scr, Ir_{en}-$AuSiO_2$_Gint4.T and Ir_{en}-$AuSiO_2$_CL4_Gint4.T was added to 0.2 mL of chloroform and 0.2 mL of TE buffer, rotated end-over-end for 90 min at RT and then centrifuged for 15 min at 13.200 rpm at 4°C. The upper phase containing the RNA was transferred to a new tube and incubated for 5 min at 37°C to remove the residual chloroform and concentrated using centrifugal filter devices (Amicon Ultra-0.5 mL 10,000 MW-cutoff centrifugal filter, Millipore, Billerica, MA). The RNA (17.5 uL) coming from each sample was reverse transcribed using Tetro Reverse Transcriptase (Bioline London, UK) and aptamer specific 3' primers. The reverse transcription protocol was as follows: the RNA and the primer were heated at 65°C for 5 min, annealed at 22°C for 5 min and extended at 42°C for 15 min followed by an extension at 50°C for 30 min and enzyme inactivation at 85°C for 5 min. The products from the reverse transcription reaction were subjected to qPCR amplification. The sequences of aptamer-specific 5' and 3' primers for Gint4.T and Scr, and CL4 were reported in [40, 43], respectively.

The conjugation efficiency was calculated as pmoles of $aptamer_{conjugated}$/ $aptamer_{total}$ (%).

Cell lines and two-dimensional (2D) culture conditions

Human MES-TNBC MDA-MB-231 and BT-549, luminal B/HER2-positive breast cancer BT-474, luminal A/estrogen receptor and progesterone receptor-positive breast cancer MCF7, and epidermoid carcinoma A431 cell lines were purchased from the American Type Culture Collection (ATCC, Manassas, VA) and grown as previously reported [44]. Green fluorescent protein (GFP)-labeled BT-549 cells (BT-549-GFP) was produced as previously described [30] and grown in Roswell Park Memorial Institute-1640 medium (Sigma-Aldrich, Milan, Italy) supplemented with 10% fetal bovine serum (Sigma-Aldrich). Human adipose MSCs were purchased from Sigma-Aldrich (SCC038) and grown in Human Mesenchymal-XF Expansion Medium (Sigma-Aldrich) in a humidified incubator in 5% CO2 at 37°C.

Establishment of 3D spheroids of stromal cells and breast cancer cells

For 3D heterotypic tumor spheroids, 2×10^3 cancer cells were mixed with 8×10^3 MSCs (ratio 1:4) and seeded in 24-ultralow attachment plates (Corning Incorporate, Corning, NY) in Dulbecco's Modified Eagle Medium (DMEM)/F-12 medium (D8437 Sigma-Aldrich), supplemented with 2% Matrigel Basement Membrane Matrix Growth Factor Reduced (Corning Incorporate), B27 (1:50, Gibco™ by Invitrogen, Carlsbad, CA), 20 ng/ml basic fibroblast growth factor (Sigma-Aldrich) and 10 ng/ml epidermal growth factor (Sigma-Aldrich). For homotypic cultures, 2×10^3 cancer cells or 8×10^3 MSCs were seeded alone. Spheroid formation was checked daily using a phase-contrast microscopy (Leica DMI3000 B apparatus), images were captured and the diameter of spheroids was measured.

Establishment of patient-derived breast cancer organoids

Breast cancer samples from three patients who underwent surgery at the National Cancer Institute "Fondazione Giovanni Pascale" of Naples, Italy, were enrolled in this study. This study was approved by the ethics committee of INT Pascale (Prot. CEI/390/15) and all the patients provided written informed consent. The tissue samples were collected for histopathological diagnosis and an aliquot was stored in the Institutional Biobank (BBI). Immunohistochemical staining was done on biobank histological formalin-fixated and paraffin-embedded tissue samples slides (4 μm), as previously reported [39], by using primary antibodies against PDGFRβ (dilution 1:50, rabbit monoclonal antibody, Cell Signaling Technology Inc., Danvers, MA). Results were interpreted using a light microscope. Ten fields on each of two cores and at least > 500 cells were analyzed for each sample. Two pathologists independently evaluated the intensity, extent and subcellular distribution of the immunostaining. PDGFRβ expression was interpreted as positive when membranous and/or cytoplasmic staining was observed. Staining was scored as follows: negative (absence of staining) and positive (≥ 1%) in tumor cells.

Organoid development methods followed a previous reported procedure study [45]. Briefly, fresh tumor specimens were collected and transported in working medium (WM), consisting of DMEM-F/12 medium (Sigma-Aldrich) supplemented with 1x Antibiotic-Antimycotic (Gibco™ by Invitrogen) and 10 μg/mL gentamycin (Euroclone, Milan, Italy), minced mechanically and then digested in WM (10 mL/g of tissue) supplemented with 2 mg/mL Collagenase Type II (Gibco™ by Invitrogen), for 16 h at 37°C under shaking. The digested tissue was filtered through a 100 μm cell strainers (Corning Incorporate) followed by a 40 μm cell strainer (Corning Incorporate) to separate organoids from single cells, and then tumor fragments

retained by the cell strainer were washed in WM. The suspension containing tumor organoids was centrifuged 5 min at 500×g and the organoid pellet was plated in 24-ultralow attachment plates (Corning Incorporate) in the culture medium previously reported [45]. After 24 h, the organoids were centrifuged again at 500×g and finally resuspended in 90% Matrigel Basement Membrane Matrix Growth Factor Reduced (Corning) diluted in WM and 35 µL drops were allowed to solidify in the inverted 24-well plates for 20 min at 37°C. Organoids-Matrigel drops were then covered with 500 µL of culture medium and transferred into incubator for culturing. The culture medium was replaced every 3–4 days and organoids were passaged every 2–3 weeks at a split ratio of 1:2–1:3 using mechanical dissociation by pipetting or enzymatic digestion using TripLE Express (Gibco™ by Invitrogen) for 5–15 min at 37°C.

Immunoblotting

Cell lysates' preparation and immunoblot analyses were performed as previously reported [35]. The filters were probed with the indicated primary antibodies: anti-EGFR, anti-PDGFRβ, anti-vinculin and anti-α-tubulin (Cell Signaling Technology Inc.). The blots shown are representative of at least three independent experiments.

Flow cytometry

PDCOs were mechanically and enzymatically disaggregated into a single-cell suspension and then incubated with anti-EGFR or anti-PDGFRβ (dilution 1:50, R&D system, Minneapolis, MN) primary antibody diluted in Dulbecco's phosphate buffered saline (DPBS)/BlockAid™ blocking solution (Invitrogen), for 15 min at RT. After three washes with DPBS, cells were incubated with Alexa Fluor 488 Anti-Goat (Invitrogen), washed three times in DPBS, suspended in 500 µl DPBS and analyzed by flow cytometry (BD Accuri™ C6). Data analysis was performed using FlowJo software (version 10.0.7).

Confocal Microscopy

To evaluate uptake of nanoparticles in 2D cell systems, MDA-MB-231, BT-549, BT-474, A431, MCF7 cells (5.0×10^4 cells/well in 24-well) or MSCs (4.0×10^4 cells/well in 24-well) were seeded on the coverslip and, after 24 h, were incubated for 30 or 60 min at 37°C with Ir_{en}-$AuSiO_2$_COOH/NHS or Ir_{en}-$AuSiO_2$_Aptamer nanoparticles, diluted at 5 µM Ir_{en} concentration in culture medium with 0.1 mg/mL yeast tRNA and 0.1 mg/mL ultrapure™ salmon sperm DNA (Invitrogen), as nonspecific competitors. After three washes with DPBS, cells were fixed with 4% paraformaldehyde in DPBS for 30 min at RT, permeabilized with 0.1% Triton X-100/DPBS for 5 min, subjected to nuclear staining with the NucRed 647 (Invitrogen), following the provider indications, and mounted with glycerol/DPBS. Wheat Germ Agglutinin-Alexa Fluor 488 conjugate (WGA-488) was used to visualize BT-549 cell membrane.

To test the ability of Ir_{en}-$AuSiO_2$_Aptamer nanoplatforms to enter 3D models, heterotypic spheroids composed of BT-549-GFP or BT-474 tumor cells mixed with MSCs, and PDCOs (~ 100–200 µm diameter) were collected, centrifuged at 500×g for 5 min, suspended in 90% Matrigel and 15-µL drops were deposited in prewarmed 8-well Chamber Slide (1 drop/well, Ibidi GmbH, Gräfelfing, Germany). Upon completed gelation, 200 µL of culture medium was added to each well. After 24 h, spheroids or PDCOs were incubated

for 24 h at 37°C with Ir_{en}-$AuSiO_2$_COOH/NHS or Ir_{en}-$AuSiO_2$_Aptamer nanoparticles, diluted at 5 μM Ir_{en} concentration in culture medium with nonspecific competitors. After three washes with DPBS, they were fixed, permeabilized and stained with NucRed 647, as described above. Finally, glycerol/DPBS was added to each well. Samples were visualized by Zeiss LSM 700 META confocal microscopy.

Photodynamic effect of nanoplatforms in 2D cell culture

MDA-MB-231, BT-549, A431, MCF7 and BT-474 (7.0×10^3 cells/well) and MSCs (4.0×10^3 cells/well) were plated in 96-well microplates (Corning Incorporate) and, after 16 h at 37°C, were either left untreated or treated for 1 h with Ir_{en}-$AuSiO_2$_COOH/NHS, Ir_{en}-$AuSiO_2$_CL4, Ir_{en}-$AuSiO_2$_Gint4.T, Ir_{en}-$AuSiO_2$_CL4_Gint4.T or Ir_{en}-$AuSiO_2$_Scr, diluted in cell culture medium at 5 μM Ir_{en} concentration, in the presence of 0.1 mg/mL yeast tRNA and 0.1 mg/mL ultrapure™ salmon sperm DNA (Invitrogen), as nonspecific competitors. After two washes with DPBS, fresh medium was added to the plate and the cells were kept in the dark or exposed to 254 nm light irradiation (maximal irradiance 4 W m − 2) for 1 h. Cell viability was evaluated 24 h after PDT treatment by Thiazolyl Blue Tetrazolium Bromide (MTT, AppliChem GmbH, Darmstadt, Germany), according to the manufacturer's protocol.

Photodynamic effect of nanoplatforms in 3D models

Heterotypic spheroids grown in 24-ultralow attachment plates up to reach a diameter of approximately 150–180 μm, were left untreated or treated for 24 h with Ir_{en}-$AuSiO_2$_CL4, Iren-$AuSiO_2$_Gint4.T, Ir_{en}-$AuSiO_2$_CL4_Gint4.T or Ir_{en}-$AuSiO_2$_Scr (5 μM Ir_{en} concentration), diluted in culture medium in the presence of nonspecific competitors (0.1 mg/mL yeast tRNA and 0.1 mg/mL ultrapure™ salmon sperm DNA, Invitrogen). After two washes with DPBS, fresh culture medium was added to the plates and spheroids, either untreated and treated with nanoparticles, were exposed to 254 nm light irradiation (maximal irradiance 4 W m − 2) for 1 h. After 24 h, spheroids with a diameter greater than 50 μm were counted in at least 5 fields per condition, to monitor spheroid destruction. For cell viability assays, heterotypic spheroids or PDCOs (~ 100–200 μm diameter) were transferred (20 μL drop *plus* 90% Matrigel) into black clear bottom 96-well plates (Corning Incorporate) that were filled with culture medium. After 24 h, spheroids or PDCOs were left untreated or treated with each nano-formulation and irradiated as reported above. Cell viability was assessed by CellTiter-Glo® 3D (ATP) luminescent assay (Promega BioSciences Inc., San Luis Obispo, CA), according to the manufacturer's protocol, using TECAN Infinite 200Pro microplate reader.

Statistical analysis

Statistical values were defined using GraphPad Prism version 6.00 by one-way analysis of variance (ANOVA) followed by Tukey's multiple comparison test. A p-value < 0.05 was considered significant for all analyses.

Results

Design, synthesis and characterization of the multifunctional Ir_{en}-$AuSiO_2$_Aptamer nanoplatforms

Multifunctional light-responsive nanoplatforms were implemented by incorporating an Iridium-based metal complex, Ir_{en}, with photosensitizing and luminescent properties [41], within the polysiloxane matrix of gold-core/silica-shell nanoparticles (Ir_{en}-$AuSiO_2$_COOH).

The preparation of Ir_{en}-$AuSiO_2$_COOH was performed according to the well-known reverse microemulsion method [46] and a schematic representation of the synthetic procedure is illustrated in Fig. 1A. In a W/O microemulsion, water nanodroplets are stabilized by surfactant molecules and dispersed in a continuous oil phase. These reverse micelles act as nanoreactors, within which the homogenous and highly reproducible synthesis of nanoparticles takes place, minimizing the batch-to-batch variability. In the first step, the reduction of tetrachloroaurate(III) to Au^0 leads to the formation of the gold core. Then, the addition of the silane precursors in alkaline environment gives rise, through hydrolysis and condensation processes, to the formation of the silica shell. The addition of the photosensitizing and luminescent Ir_{en} before the start of the polymerization process, ensures its physical incorporation into the polysiloxane matrix. Finally, the nanoparticles surface was functionalized with a coating agent containing a siloxy alkyl chain with a terminal carboxyl group. The full characterization of the Ir_{en}-$AuSiO_2$_COOH nanoparticles, morphological features, surface charge, optical properties, photosensitizing and thermoplasmonic abilities, was reported in the Supplementary Information. TEM images revealed a homogeneous population of spherical gold-core/silica-shell particles, with an average size of 49.13 ± 4.28 nm and a gold core of 6.31 ± 0.81 nm (Supplementary Fig. 1A). Ir_{en}-$AuSiO_2$_COOH are characterized by a hydrodynamic diameter of 85.51 ± 1.17 nm, Polydispersity Index (PDI) of 0.148 and a negative ζ-potential value of -23.5 ± 3.95 mV (Supplementary Fig. 1B). Similar ζ-potential values are reported for silica surfaces functionalized with terminal carboxyl groups in neutral aqueous medium [47, 48]. The successful loading of Ir_{en} within the nanoparticle silica shell was confirmed by UV-Vis spectroscopy (Supplementary Fig. 1C,D). In particular, the extinction spectrum of the colloidal solution of Ir_{en}-$AuSiO_2$_COOH shows a broad band centered at 520 nm, corresponding to the characteristic Localized Surface Plasmon Resonance (LSPR) of the spherical gold core [49], and a more intense absorption band at lower wavelengths (250–300 nm), due to electronic transitions involving the Ir_{en} molecule [41]. Under light excitation, the emission spectrum of Ir_{en}-$AuSiO_2$_COOH presents the characteristic band of the Iridium compound, peaked at 520 nm. The goodness of the emission spectrum was confirmed by the excitation one (Supplementary Fig. 1D).

In order to validate the photo-triggered properties of the obtained nanoplatforms, light-induced singlet oxygen generation and photothermal effects were assessed (see Supplementary Information for details). In particular, the singlet oxygen generation capability was evaluated by chemical method using 9,10-Anthracenediyl-bis(methylene)dimalonic acid (ABDA) as detection probe [50]. The photooxidation of ABDA in presence of Ir_{en}-$AuSiO_2$_COOH was monitored by measuring its absorbance at 378 nm; while the absorbance attenuation of ABDA was negligible for the control solution (see Supplementary Information and Supplementary Fig. 2A), in presence of Ir_{en}-$AuSiO_2$_COOH, the absorption decreased significantly with the extension of the irradiation time (Supplementary Fig. 2B). For an immediate comparison, the ABDA absorbance values as function of the irradiation time were plotted (Supplementary Fig. 2C) and for both solutions (control and sample) a good linear relationship was observed.

The heat generation of the nanoplatforms under continuous illumination was investigated (Supplementary Information). As clearly demonstrated by the thermal images acquired after an irradiation time of 90 min (Supplementary Fig. 3), in the case of the control solution (see Supplementary Information for its description), a non-significant temperature variation was observed, whereas in the case of Ir_{en}-$AuSiO_2$_COOH, a photothermal heating of the irradiated solution as well as the surrounding environment was highlighted. The observed thermoplasmonic effect can be explained as a result of a photothermal conversion of the energy absorbed by Ir_{en} molecules and partially transferred to the metal nanoparticle. In particular, the evidenced spectral overlap between the emission band of the Iridium compound and the LSPR of the gold core, allows donor-acceptor energy transfer processes, from the Iridium-based molecules to the gold core, which in turn converts the received energy into heat [51]. Therefore, using a single excitation wavelength in the Ir_{en} absorption region, Ir_{en}-$AuSiO_2$_COOH nanoplatforms can act as luminescent probes, photosensitizing agents, and heat nanosources.

In order to specifically address Ir_{en}-$AuSiO_2$_COOH to target tumor/stromal cells, conjugation with the EGFR CL4 (Ir_{en}-$AuSiO_2$_CL4) or PDGFRβ Gint4.T (Ir_{en}-$AuSiO_2$_Gint4.T) aptamers, and dual functionalization with both CL4 and Gint4.T (Ir_{en}-$AuSiO_2$_CL4_Gint4.T) were performed. Ir_{en}-$AuSiO_2$_Scr, decorated with a non-targeting scrambled aptamer, were used as a negative control. The schematic representation of the synthetic steps involved in the development of the aptamers-conjugated gold-silica nanoplatforms and a key illustration of all the prepared samples is shown in Fig. 1B,C. Specifically, to obtain aptamers-nanoplatforms conjugates (Ir_{en}-$AuSiO_2$_Aptamer), the free –COOH groups of Ir_{en}-$AuSiO_2$_COOH were activated - through EDC/NHS chemistry [52, 53] - to react with the 5' NH_2-aptamers, with consequent formation of amide bonds (– CO–NH–). In particular, EDC reacts with a carboxylic group on nanoparticles surface, resulting in an amine-reactive O-acylisourea intermediate. The addition of NHS stabilizes the amine-reactive intermediate by converting it to an amine-reactive NHS ester. Then, through a nucleophilic attack the NHS ester is easily displaced by the amine group on the 5'-end of aptamer to yield a stable amide bond (Fig. 1B). Extinction spectra of Ir_{en}-$AuSiO_2$_COOH/NHS and all conjugated samples are displayed in Fig. 2A. Where the spectral profile of Ir_{en}-$AuSiO_2$_COOH/NHS results superimposable on the extinction spectrum of Ir_{en}-$AuSiO_2$_COOH (Supplementary Fig. 1C), in the case of Ir_{en}-$AuSiO_2$_CL4, Ir_{en}-$AuSiO_2$_Scr, Ir_{en}-$AuSiO_2$_Gint4.T and Ir_{en}-$AuSiO_2$_CL4_Gint4.T, a shoulder at 260 nm - characteristic of the maximum absorption peak of RNA sequences [54] - was observed. This absorption feature proves the successful RNA functionalization.

The DLS results (Fig. 2B,C, Supplementary Table 1) reported that the Ir_{en}-$AuSiO_2$_COOH/NHS nanoplatforms were characterized by a hydrodynamic diameter equal to 102.0 ± 0.15 nm (PDI of 0.172) and a negative ζ-potential value of -26.0 mV. Ir_{en}-$AuSiO_2$_CL4 and Ir_{en}-$AuSiO_2$_Scr were characterized by a hydrodynamic diameter of 102.1 ± 0.93 nm (PDI = 0.163) and 101.4 ± 0.20 nm (PDI = 0.162), respectively, and a negative ζ-potential value of -22.3 and − 22.9 mV each. Ir_{en}-$AuSiO_2$_Gint4.T and Ir_{en}-$AuSiO_2$_CL4_Gint4.T were characterized by a hydrodynamic diameter equal to 104.4 ± 0.47 nm (PDI = 0.168) and 103.7 ± 0.82 nm (PDI = 0.162), respectively, and a negative ζ-potential value of -28.3 and − 26.4 mV each. Therefore, Ir_{en}-$AuSiO_2$_COOH/NHS as well as all Ir_{en}-$AuSiO_2$_Aptamer samples have a hydrodynamic diameter very similar

to each other. However, these values are larger than that of Ir_{en}-$AuSiO_2$_COOH, plausibly due to variations in the surface coating and/or hydration sphere. Conversely, no significant changes were observed in the surface charge values of all the nanoplatforms (Ir_{en}-$AuSiO_2$_COOH, Ir_{en}-$AuSiO_2$_COOH/NHS, Ir_{en}-$AuSiO_2$_Aptamer), as result in all cases of an extensive presence of free carboxyl groups on the surface of the nanoplatforms. The amount of each aptamer conjugated to the nanoplatforms was evaluated by RT-qPCR analysis on Ir_{en}-$AuSiO_2$_Aptamer (Supplementary Fig. 4). We quantified approximately 3.0 pmol aptamer per 16.0 pmol of Ir_{en}-$AuSiO_2$_ Aptamer nanoplatform and the efficiency of conjugation ranged between 2% and 6% with a mean ± SEM equal to 4 ± 2%.

2D cell imaging by Ir_{en}-$AuSiO_2$_Aptamer nanoplatforms

To assess the cell targeting/uptake ability of nanoparticles conjugated to a single aptamer, CL4 or Gint4.T, or functionalized to both aptamers, we took advantage of different human cell lines expressing only EGFR, only PDGFRβ, both, or neither of the receptors. Specifically, human MES-TNBC MDA-MB-231 and BT-549 cells were chosen as double-positive cells as they express both EGFR and PDGFRβ ([23] and Supplementary Fig. 5) and, consequently, are specifically targeted by the two aptamers either when grown in classical 2D cultures and 3D Matrigel-embedded cultures, or implanted in mice [23, 30, 39]. Furthermore, we previously proved that CL4 strongly improves the uptake of drug-loaded and aptamer-decorated poly(lactic-co-glycolic)-poly ethylene glycol-based nanoparticles into both cell lines in vitro and in vivo [24]. As models of $EGFR^+/PDGFR\beta^-$ cell lines, we used breast cancer BT-474 and epidermoid carcinoma A431 cell lines, which express moderate and high levels of EGFR, respectively, without expressing PDGFRβ ([23, 44] and Supplementary Fig. 5), and are thus recognized by CL4 [19] but not Gint4.T [35, 39]. Moreover, stromal MSCs that express high levels of PDGFRβ were selected as $EGFR^-/PDGFR\beta^+$ cells ([30, 55] and Supplementary Fig. 5). Importantly, we previously demonstrated that Gint4.T, by blocking PDGFRβ, efficiently inhibits MSCs recruitment into TNBC thus preventing their pro-metastatic function [30]. Finally, $EGFR^-/PDGFR\beta^-$ breast cancer MCF7 cells ([23] and Supplementary Fig. 5) were used as a negative control.

The intrinsic green (Iridium-compound associated) fluorescence emitted from the unconjugated Ir_{en}-$AuSiO_2$_COOH/NHS or Ir_{en}-$AuSiO_2$_Aptamer nanoplatforms (5 μM Ir_{en} concentration) was collected by confocal microscopy after incubation of the cells with the nanoparticles at 37°C in the presence of yeast tRNA and salmon sperm DNA competitors to hinder any non-specific interactions. As shown (Fig. 3A), the signal associated with Ir_{en}-$AuSiO_2$_Aptamer (Ir_{en}-$AuSiO_2$_CL4, Ir_{en}-$AuSiO_2$_Gint4.T and Ir_{en}-$AuSiO_2$_CL4_Gint4.T) nanoparticles was clearly visible in the cytoplasm of MDA-MB-231 cells at 30 min and further increased at 60 min of incubation. Conversely, an almost undetectable signal was obtained with unconjugated Ir_{en}-$AuSiO_2$_COOH/NHS or scrambled decorated Ir_{en}-$AuSiO_2$_Scr nanoparticles at the two incubation times. Importantly, MDA-MB-231 cells treated with the dual-targeting EGFR/PDGFRβ nanoparticles had significantly higher fluorescence intensity than that treated with single-targeting EGFR or PDGFRβ nanoparticles (Fig. 3A), indicating that CL4 and Gint4.T, simultaneously attached to the nanoparticles, confer improved cellular uptake. Similar results were observed on $EGFR^+/PDGFR\beta^+$ BT-549 cells (Fig. 3A). Labeling cells with WGA to visualize cell membrane confirmed that the CL4 and Gint4.T

aptamers properly drive the nanoparticles in the cytoplasm (Supplementary Fig. 6A). As expected, no signal was observed in double negative MCF7 control cells (Fig. 3A).

As a next step, the nanoparticle' formulations were incubated for 60 min onto only $EGFR^+$ A431 (Fig. 3B) and BT-474 (Supplementary Fig. 6B) cell lines, and only $PDGFR\beta^+$ MSCs (Fig. 3C), and confocal microscopy analyses revealed that the internalization ability of the nanoparticles strictly depends on the aptamer present on the nanoparticle's surface and the expression of its receptor partner on the target cell.

Overall, these results show efficient capability of Ir_{en}-$AuSiO_2$_Aptamer nanoparticles to selectively enter into the cell through EGFR and/or PDGFRβ recognition and indicate that the carriers' parameters, including composition, size, shape and surface chemistry, do not affect the interactions of CL4 and Gint4.T aptamers to their proper receptor on membranes of target cells.

Uptake of Ir_{en}-$AuSiO_2$_Aptamer nanoplatforms in 3D multicellular tumor spheroids

Next, we wondered whether multifunctional nanoparticles retain their targeting ability in more relevant in vitro cancer models by using 3D multicellular spheroids obtained by co-culturing tumor and stromal cells on non-adhesive culture dishes, which resemble the organization and properties of a native tumor, as a key factor of translational medicine [56, 57]. Even if these models have been successfully used to study tumor-MSC interaction [56, 57], to date a still limited number of studies have employed 3D tumor spheroids for evaluating the functionality of nanomedicine [58].

In order to distinguish cancer cells from stromal cells we established tumor spheroids consisting of GFP-labeled BT-549 and unlabeled MSCs. In agreement with previous findings, both BT-549 cells [59, 60] and MSCs [61, 62] were able to form spheroids alone in non-attached culture (Supplementary Fig. 7). When cancer cells were co-cultured with stromal cells at a 1:4 ratio, respectively [63], consistent heterotypic spheroids (BT-549 + MSCs), were obtained, reaching approximately 180 μm in diameter, in 13 days (Supplementary Fig. 7 and Fig. 4A). In order to better visualize formed spheroids, they were embedded in Matrigel and observed by confocal microscopy (Fig. 4B). NucRed 647 nuclear stain was used to visualize both cancer and stromal cells, while the GFP to visualize cancer cells. As shown (Fig. 4B), the presence of NucRed 647 nuclear stain (visualized in blue) either associated to the GFP signal (BT-549) or not (MSCs) (see arrows in the merged image), indicates the mixed composition of the spheroids. To examine the penetration of the different nanoformulations into the spheroids, BT-549/MSCs spheroids were exposed to Ir_{en}-$AuSiO_2$_Aptamer and unconjugated nanoparticles, at an Ir_{en} concentration of 5 μM, for 24 h at 37°C and visualized by confocal microscopy (Fig. 4C). Importantly, the presence of the EGFR and PDGFRβ targeting aptamers on the surface of the nanoparticles, either single-targeted (Ir_{en}-$AuSiO_2$_CL4 and Ir_{en}-$AuSiO_2$_Gint4.T) or dual-targeted (Ir_{en}-$AuSiO_2$_CL4_Gint4.T), allowed them to penetrate the mixed tumor/stromal spheroids as qualitatively displayed by the nanoplatform-associated fluorescent signal (visualized in red) that was visible throughout the spheroids. 3D images clearly indicated the accumulation of the aptamer-functionalized nanoparticles inside the spheroid mass. Conversely, no signal was detected with unconjugated Ir_{en}-$AuSiO_2$ or Ir_{en}-$AuSiO_2$_Scr negative control (Fig. 4C), thus indicating that passive

infiltration of the spheroids by untargeted nanoparticles could not occur at least under the experimental conditions used.

Anticancer photokilling activity of Ir_{en}-$AuSiO_2$_Aptamer nanoplatforms in 3D multicellular tumor spheroids

We wondered whether the nanoparticles conjugated to CL4, Gint4.T or both the aptamers, once penetrated into the spheroids, kill cancer and stromal cells upon light irradiation. Thus, we first validated that $AuSiO_2$_COOH/NHS, $AuSiO_2$_Scr, $AuSiO_2$_CL4 or $AuSiO_2$_Gint4.T nanoparticles, which had no load of photosensitizing and luminescent molecule Ir_{en}, when incubated for 24 h at 37°C on MDA-MB-231 and BT-549 cells have no adverse effects on cell viability (Supplementary Fig. 8A,B).

Next, before moving on to more complex 3D cell systems, we verified the therapeutic efficacy of Ir_{en}-loaded nanoformulations in 2D cell cultures. To this aim, BT-549 and MDA-MB-231, positive for EGFR and PDGFRβ, BT-474 and A431, positive for EGFR, MSCs, positive for PDGFRβ, and MCF7 cells, negative for both receptors, were incubated with the different nanoformulations containing Ir_{en} (5 μM) and decorated or not with the aptamers, for 1 h, given the rapid cell uptake of aptamer-decorated nanoparticles, washed to remove not-internalized nanoparticles, exposed to 1-h light irradiation and analyzed for their viability after 24 h. As shown (Supplementary Fig. 8C-H), Ir_{en}-$AuSiO_2$_Aptamer nanoplatforms demonstrated efficient capability to selectively kill the cells, through EGFR and/or PDGFRβ recognition, in comparison with untargeted NPs (unconjugated Ir_{en}-$AuSiO_2$_ COOH/NHS or scrambled-conjugated Ir_{en}-$AuSiO_2$_Scr). No toxicity of aptamer-decorated nanoplatforms was observed on each cell line under dark conditions, thus indicating their safety behavior at least in the concentrations tested in the PDT experiments.

Importantly, when incubated for 24 h with heterotypic BT-549 + MSCs spheroids, Ir_{en}-$AuSiO_2$_CL4, Ir_{en}-$AuSiO_2$_Gint4.T and Ir_{en}-$AuSiO_2$_CL4_Gint4.T (5 μM Ir_{en} concentration; 1-h light irradiation), disrupted spheroid structure (Fig. 5A,B) and inhibited cell viability (Fig. 5C), as determined by spheroids number counting and CellTiter-Glo 3D cell viability assay, respectively, with the dual targeted nanoparticles being more effective than the single-targeted ones (approximately 80% inhibition, Ir_{en}-$AuSiO_2$_CL4_Gint4.T *vs* 40% inhibition, Ir_{en}-$AuSiO_2$_CL4, and 50% inhibition, Ir_{en}-$AuSiO_2$_Gint4.T). Conversely, no effect was observed on controls consisting of untreated or treated with scrambled-decorated Ir_{en}-$AuSiO_2$ nanoformulations spheroids (Fig. 5A-C). Similarly, a higher effect on cell viability inhibition was observed upon treatment of heterotypic MDA-MB-231 + MSCs spheroids with Ir_{en}-$AuSiO_2$_CL4_Gint4.T compared to single-targeted nanoparticles (Fig. 5D,E).

Because MES-TNBC cells express both EGFR and PDGFRβ, in order to confirm the efficacy of the dual-targeting nanovectors on both cancer and stromal cells, we generated tumor spheroids consisting of cancer BT-474 cells (only $EGFR^+$) and MSCs (only $PDGFR\beta^+$) that grew as colonies with approximately a 150 μm diameter after 13 days in culture (Supplementary Fig. 9A and Fig. 6A). As shown, uptake into BT-474/MSCs spheroids of either single-targeted Ir_{en}-$AuSiO_2$_CL4 and Ir_{en}-$AuSiO_2$_Gint4.T, as well as dual-targeted Ir_{en}-

$AuSiO_2$_CL4_Gint4.T nanoparticles after 24 h of incubation was clearly detected by confocal microscopy (Fig. 6B) and the cytotoxic effect of Ir_{en}-$AuSiO_2$_CL4_Gint4.T nanoparticles on both the spheroid disruption (Fig. 6C,D) and cell viability inhibition (Fig. 6E) was higher than that of either Ir_{en}-$AuSiO_2$_CL4 or Ir_{en}-$AuSiO_2$_Gint4.T (approximately 70% inhibition for Ir_{en}-$AuSiO_2$_CL4_Gint4.T *vs* 40% inhibition for Ir_{en}-$AuSiO_2$_CL4 and Ir_{en}-$AuSiO_2$_Gint4.T, relative to untreated cultures), thus confirming the ability of dual-decorated nanoparticles to kill both cancer and stromal cells through EGFR and PDGFRβ targeting, respectively.

Similarly, tumor spheroids consisting of A431 cells (only $EGFR^+$) grown with MSCs (only $PDGFR\beta^+$) up to 13 days (Supplementary Fig. 9B and Fig. 6F) were higher affected by EGFR/PDGFRβ bispecific nanoformulations than those single-targeted, with a reduction of cell viability of approximately 90% for Ir_{en}-AuSiO2_CL4_Gint4.T, 40% for Ir_{en}-$AuSiO_2$_CL4 and 30% for Ir_{en}-$AuSiO_2$_Gint4.T relative to untreated cultures (Fig. 6G).

Anticancer photokilling activity of Ir_{en}-$AuSiO_2$_Aptamer nanoplatforms on 3D patient-derived cancer organoids

To further prove the targeting efficacy and the photoinduced killing activity of dual aptamer-decorated nanoparticles, through selective recognition of EGFR-positive tumor cells and PDGFRβ-positive stromal component in the entire tumor bulk, we employed 3D patient organoids from human surgical specimens collected from three patients with diagnosis of breast cancer. Tumor samples, henceforth named M23, M41 and M43, were chosen for the absence of PDGFRβ expression in tumor cells (blue arrows) and its presence in the stromal component, specifically in vascular endothelial cells (green arrows) and/or mesenchymal stromal cells (orange arrows) (Fig. 7A), as assessed by immunohistochemical analyses. The clinical pathological characteristics of the three tumors are summarized in the Supplementary Table 2. PDCOs at the first passage were cultured up to day 10 (Fig. 7B, upper panels), disaggregated into a single-cell suspension and analyzed by flow cytometry to confirm the expression of EGFR on epithelial tumor cells and PDGFRβ on stromal cells (Fig. 7B, lower panels). Confirming results obtained in 3D multicellular tumor spheroids, Ir_{en}-$AuSiO_2$_Aptamer nanoplatforms efficiently spread into the organoid mass (Fig. 7C) and exert excellent anticancer photokilling activity, which was superior with the dual-aptamer-decorated nanoparticles over single-aptamer-conjugated (Fig. 7D). Conversely, no effect was observed in untreated organoids or those treated with scrambled-aptamer-conjugated nanoparticles (Fig. 7D).

Taken together, our results show the striking antitumor potential of our bispecific light-triggered nanoplatforms targeting tumor and stromal cells and highlight the potential translational value of integrative research combining patient-derived organoids and cancer nanomedicine.

Discussion

In breast cancer development, as in many other human tumors, stromal cells contribute to the establishment of a supportive microenvironment for tumor cells. Tumor-stroma cross-talk promotes

angiogenesis, immune evasion, and extracellular matrix remodeling, creating a favorable niche for cancer cell growth. Additionally, stromal cells can influence the behavior of tumor cells, impacting their ability to invade surrounding tissues and metastasize to distant organs [4]. Therapeutically, understanding and targeting the interactions between stroma and tumor cells have become essential strategies. The TME, rich in stromal components, can contribute to treatment resistance and limit the effectiveness of therapies targeting tumor cells alone [1]. Therefore, therapies that take into account the dynamic interplay between stroma and tumor cells are gaining attention.

Organoids and 3D coculture models of tumor and stromal cells have emerged as powerful tools in cancer therapy research, providing more physiologically relevant and predictive platforms compared to traditional 2D cell cultures. The importance of these advanced models lies in their ability to better recapitulate the complexity of the tumor that is dependent on its TME, offering insights into tumor-stromal interactions and improving the translational potential of preclinical studies [8].

Here we focus on the design and evaluation of bispecific nanotherapeutics that selectively act on both tumor and stromal cells, presenting a promising strategy to advance the outcome of traditional tumor cell-targeting nanomedicine by influencing the tumor-supporting activity of stromal cells in the complex TME.

Cell targeting agents are crucial components of targeting delivery systems, and oligonucleotide aptamers represent the best choice because of their stability, ease of manufacture at high reproducibility, and low or absent immunogenicity. Moreover, their chemical synthesis and versatility for chemical modification allows easier conjugation to different kinds of nanoplatforms, at higher yield and lower costs, than other form of ligands as antibodies or peptides [28, 64], which is relevant for industrial scale up. To date, a limited number of dual-aptamer modified nanoplatforms have been developed for achieving cancer therapeutic efficacy superior to that of single targeting through the recognition of different tumor cell types [65, 66] or different receptors on the same tumor cells [67, 68] and, to the best of our knowledge, this is the first study exploring bispecific nanoparticles with two different aptamers for exerting excellent anti-tumor cytotoxic effects on both tumor cells and the reactive stroma.

We prepared gold-core/silica-shell nanoparticles via reverse microemulsion method, an ideal synthetic approach to get spherical and highly monodispersed particles. The presence of the Iridium compound in the polysiloxane matrix gives the nanostructure photosensitizing and luminescent capabilities, while that of the gold-core ensures photothermal properties. The nanoparticle surface containing carboxyl groups was decorated with amino-terminated EGFR (CL4) and PDGFRβ (Gint4.T) aptamers, through the formation of amide bonds, creating a multifunctional nanoplatform termed Ir_{en}-AuSiO_2_CL4_Gint4.T. The specificity and synergistic effects of these dual-aptamer-decorated nanoparticles were rigorously assessed through confocal microscopy and cell viability assays on various human cell types, including TNBC cell lines, luminal/HER2-positive breast cancer cells, epidermoid carcinoma cells, and adipose-derived mesenchymal stromal/stem cells, and preclinical 3D stroma-rich breast cancer models, consisting of either 3D spheroids cocultures of tumor cells and MSCs, and breast cancer organoids derived from pathologically and molecularly well-characterized human tumors. Crucially, the results demonstrate the efficient capability of aptamer-conjugated nanoplatforms not only to selectively enter target cells and induce cell death in 2D cell

cultures but also uniformly spread into both breast cancer spheroids and organoids and disrupt them through recognition of $EGFR^+$ tumor cells and $PDGFR\beta^+$ stromal cells, highlighting the superiority of dual-aptamer-decorated nanoparticles over single-aptamer-conjugated counterparts.

Notably, EGFR is a well characterized surface molecule for epithelial cells in many types of cancers and, accordingly, we and other groups worldwide have successfully applied the EGFR CL4 aptamer as tumor ligand to decorate nanocarriers actively targeted to TNBC [24–27, 69, 70], hepatocellular carcinoma [68], osteosarcoma [65] and chordoma [71]. Based on these observations, our bispecific Ir_{en}-$AuSiO_2$_CL4_Gint4.T nanoparticles could be safely applied not only to breast cancer PDO, as in the present study, but also several others EGFR-expressing cancers. At the same time, the proposed strategy for aptamer-functionalized nanoformulation can be easily adapted to different targets by switching the aptamers for other malignant tumors.

Also, we proved that the Gint4.T aptamer, by binding to PDGFRβ expressed both on tumor cells and immune populations enhances the efficacy of anti-programmed cell death-ligand 1 monoclonal antibodies in inhibiting tumor growth and metastasis formation in a syngeneic TNBC mouse model [35]. Thus, immuno- and targeted therapy may be easily combined with our aptamer-targeted nanomedicine for synergistically targeting either tumor and immune cells.

Moreover, in the context of highly aggressive human cancers, including MES-TNBC [39, 72] and different glioblastoma (GBM) subtypes [73], being characterized by a strong PDGFRβ-positivity on tumor cells and self-renewing stem cells, Ir_{en}-$AuSiO_2$_CL4_Gint4.T may act in a synergistic way by targeting either EGFR and PDGFRβ on the epithelial tumor cells and PDGFRβ in the stroma components. At this regards, different therapeutic nanoformulations have been reported for GBM targeting that exploit Gint4.T aptamer as a potent ligand with the capability of not only passing through the blood-brain barrier by transcytosis but also recognizing the cancer cell membrane [40, 74–76].

One important result of this study is the absence of cell toxicity of our aptamer-decorated nanoformulations in the absence of light irradiation in either 2D cell cultures and in 3D systems, including both heterotypic spheroids and breast cancer patient organoids, thus suggesting them as an effective and safe anti-tumor strategy in clinical settings. Further investigation in humanized mice models will be performed to assess the pharmacokinetic and pharmacodynamic profile of the proposed nanomedicine along with their therapeutic efficacy, opening new avenues for innovative therapeutics in the realm of personalized medicine.

Conclusions

The dynamic interplay between the tumor cells and the stroma is critical for promoting tumor growth and progression, and dictate resistance to therapies. In summary, we have proposed new dual aptamer-equipped nanoformulations that combine anticancer and anti-stroma targeting for precision phototherapeutic applications. Albeit biodistribution and efficacy of the nanoplatforms need to be addressed in vivo, our results clearly indicate their high potential as efficient tools for precision phototherapies of breast cancers with overexpression of EGFR and likely other human tumors.

Abbreviations

2D: Two-Dimensional

2'F-Py: 2'-Fluoro-pyrimidines

3D: Three-Dimensional

ABDA: 9,10-Anthracenediyl-bis(methylene)dimalonic acid

APTES: (3-aminopropyl)triethoxysilane

DLS: Dynamic Light Scattering

DMEM: Dulbecco's Modified Eagle Medium

DPBS: Dulbecco’s Phosphate Buffered Saline

EDC: N-(3-dimethylaminopropyl)-N'-ethylcarbodiimide hydrochloride

EGFR: Epidermal Growth Factor Receptor

GBM: Glioblastoma

GFP: Green Fluorescent Protein

HER2: Human Epidermal Growth Factor Receptor 2

Ir_{en}: Iridium(III) compound ethylenediamine

LSPR: Localized Surface Plasmon Resonance

MES: Mesenchymal Subtype

Mesna: Sodium 2-mercaptoethanesulfonate

MFI: Mean fluorescence intensity

MSCs: Adipose-derived Mesenchymal Stromal/Stem Cells

NHS: N-hydroxysuccinimide

PBS: Phosphate Buffer Solution

PDCOs: Patient-Derived Cancer Organoids

PDGFRβ: Platelet-Derived Growth Factor Receptor β

PDI: Polydispersity Index

PDT: Photodynamic Therapy

PTT: Photothermal Therapy

RT: Room Temperature

RT-qPCR: Reverse Transcription-Quantitative Polymerase Chain Reaction

TEM: Transmission Electron Microscopy

TEOS: Tetraethoxysilane

TME: Tumor Microenvironment

TNBC: Triple-Negative Breast Cancer

WGA: Wheat Germ Agglutinin

WM: Working Medium

W/O: Water/Oil

Declarations

Acknowledgements

Institutional Biobank (BBI) of INT IRCCS Pascale is acknowledged. University of Campania "Luigi Vanvitelli", which coordinates the PhD program followed by LA is acknowledged.

Authors' contributions

LC conceived and supervised the study; SC, AC, LA performed in vitro cell experiments and ex vivo experiments on PDCO; EM, MM, MLD and LR developed and characterized the nanoparticles; MC (Monica Cantile) provided clinical specimens; MC (Margherita Cerrone) performed immunohistochemical staining; SC, AZ, MF, MLD, LR and LC analyzed the data, discussed the results and provided critical review; LC was responsible for funding; LC and LR wrote the original draft; all authors contributed to and approved the final version of the manuscript.

Funding

The research leading to these results has received funding from AIRC under IG 2019 - ID. 23052 project – P.I. LC, and the European Union – Next Generation EU for the PNRR project CN00000041 "National Center for Gene Therapy and Drugs based on RNA Technology", CUP "B83C22002860006" to LC.

LA was supported by AIRC fellowship for Italy, project code 26742.

Availability of data and materials

All data analyzed during this study are included in this manuscript.

Ethics approval and consent to participate

This study was approved by the ethics committee of INT Pascale (Prot. CEI/390/15) and all the patients provided written informed consent.

Consent for publication

Not applicable.

Competing interests

The authors declare that they have no competing interests.

Author details

[1]Institute of Experimental Endocrinology and Oncology "Gaetano Salvatore", National Research Council, 80131, Naples, Italy. [2]CNR-NANOTEC Institute of Nanotechnology, National Research Council, Rende (CS), Italy. [3]Department of Chemistry and Chemical Technologies, University of Calabria, Rende (CS), Italy. [4]Department of Chemistry, Biology and Biotechnology, University of Perugia, Italy. [5]Institute of Light and Matter, Claude Bernard University Lyon 1, UMR 5306, Villeurbanne, France. [6]Institutional Biobank-Scientific Directorate, National Cancer Institute INT-IRCCS Fondazione G. Pascale, 80131, Naples, Italy. [7]Pathology Unit, National Cancer Institute INT-IRCCS Fondazione G. Pascale, 80131, Naples, Italy. [8]Institute of Biostructures and Bioimaging, National Research Council, 80145, Naples, Italy.

References

1. Tiwari A, Trivedi R, Lin SY. Tumor microenvironment: barrier or opportunity towards effective cancer therapy. J Biomed Sci. 2022;29:83.
2. Mueller MM, Fusenig NE. Friends or foes - bipolar effects of the tumour stroma in cancer. Nat Rev Cancer. 2004;4:839–49.
3. Fang H, Declerck YA. Targeting the tumor microenvironment: from understanding pathways to effective clinical trials. Cancer Res. 2013;73:4965–77.
4. Tu Z, Karnoub AE. Mesenchymal stem/stromal cells in breast cancer development and management. Semin Cancer Biol. 2022;86:81–92.
5. Millard M, Yakavets I, Zorin V, Kulmukhamedova A, Marchal S, Bezdetnaya L. Drug delivery to solid tumors: the predictive value of the multicellular tumor spheroid model for nanomedicine screening. Int J Nanomed. 2017;12:7993–8007.
6. Matthew JW, Vazrik K, Justin JL, Jason CH, Carlos AF, Paul R, et al. Generation of an in vitro 3D PDAC stroma rich spheroid model. Biomaterials. 2016;108:129–42.

7. Zhao Z, Chen X, Dowbaj AM, Sljukic A, Bratlie K, Lin L, et al. Organoids Nat Rev Methods Primers. 2022;2:94.
8. Jiang S, Deng T, Cheng H, Liu W, Shi D, Yuan J, et al. Macrophage-organoid co-culture model for identifying treatment strategies against macrophage-related gemcitabine resistance. J Exp Clin Cancer Res. 2023;42:199.
9. Jing Z, Du Q, Zhang X, Zhang Y. Nanomedicines and nanomaterials for cancer therapy: Progress, challenge and perspectives. Chem Eng J. 2022;446:137147.
10. Zhang X, Wang S, Cheng G, Yu P, Chang J. Light-Responsive Nanomaterials for Cancer Therapy. Engineering. 2022;13:18–30.
11. Gai S, Yang G, Yang P, He F, Lin J, Jin D, et al. Recent advances in functional nanomaterials for light–triggered cancer therapy. Nano Today. 2018;19:146–87.
12. Ricciardi L, La Deda M. Recent advances in cancer photo-theranostics: the synergistic combination of transition metal complexes and gold nanostructures. SN Appl Sci. 2021;3:372.
13. Yu XT, Sui SY, He YX, Yu CH, Peng Q. Nanomaterials-based photosensitizers and delivery systems for photodynamic cancer therapy. Biomater Adv. 2022;135:212725.
14. Xie J, Wang Y, Choi W, Jangili P, Ge Y, Xu Y, et al. Overcoming barriers in photodynamic therapy harnessing nano-formulation strategies. Chem Soc Rev. 2021;50:9152–201.
15. Xie Z, Fan T, An J, Choi W, Duo Y, Ge Y, et al. Emerging combination strategies with phototherapy in cancer nanomedicine. Chem Soc Rev. 2020;49:8065–87.
16. He Z, Zhang CY, Lei Y, Song G, Yao Y. Plasmonic nanomaterials: A versatile phototheranostic platform of cancers. Mater Today. 2023;62:168–89.
17. Ricciardi L, Sancey L, Palermo G, Termine R, De Luca A, Szerb EI, et al. Plasmon-mediated cancer phototherapy: the combined effect of thermal and photodynamic processes. Nanoscale. 2017;9:19279–89.
18. Ricciardi L, Chatterjee S, Palermo G, Szerb EI, Sanna A, Palermo F, et al. Hybrid Nanoparticles as Theranostics Platforms for Glioblastoma Treatment: Phototherapeutic and X-ray Phase Contrast Tomography Investigations. JNT. 2022;3:1–17.
19. Esposito CL, Passaro D, Longobardo I, Condorelli G, Marotta P, Affuso A, et al. A neutralizing RNA aptamer against EGFR causes selective apoptotic cell death. PLoS ONE. 2011;6:e24071.
20. Camorani S, Esposito CL, Rienzo A, Catuogno S, Iaboni M, Condorelli G, et al. Inhibition of receptor signaling and of glioblastoma-derived tumor growth by a novel PDGFRβ aptamer. Mol Ther. 2014;22:828–41.
21. Passariello M, Camorani S, Vetrei C, Cerchia L, De Lorenzo C. Novel Human Bispecific Aptamer-Antibody Conjugates for Efficient Cancer Cell Killing. Cancers (Basel). 2019;11:1268.
22. Passariello M, Camorani S, Vetrei C, Ricci S, Cerchia L, De Lorenzo C. Ipilimumab and Its Derived EGFR Aptamer-Based Conjugate Induce Efficient NK Cell Activation against Cancer Cells. Cancers (Basel). 2020;12:331.

23. Camorani S, Crescenzi E, Gramanzini M, Fedele M, Zannetti A, Cerchia L. Aptamer-mediated impairment of EGFR-integrin αvβ3 complex inhibits vasculogenic mimicry and growth of triple-negative breast cancers. Sci Rep. 2017;7:46659.
24. Agnello L, Tortorella S, d'Argenio A, Carbone C, Camorani S, Locatelli E, et al. Optimizing cisplatin delivery to triple-negative breast cancer through novel EGFR aptamer-conjugated polymeric nanovectors. J Exp Clin Cancer Res. 2021;40:239.
25. Shu D, Li H, Shu Y, Xiong G, Carson WE 3rd, Haque F, et al. Systemic Delivery of Anti-miRNA for Suppression of Triple Negative Breast Cancer Utilizing RNA Nanotechnology. ACS Nano. 2015;9:9731–40.
26. Zhang L, Mu C, Zhang T, Yang D, Wang C, Chen Q, et al. Development of targeted therapy therapeutics to sensitize triple-negative breast cancer chemosensitivity utilizing bacteriophage phi29 derived packaging RNA. J Nanobiotechnol. 2021;19:13.
27. Guo S, Vieweger M, Zhang K, Yin H, Wang H, Li X, et al. Ultra-thermostable RNA nanoparticles for solubilizing and high-yield loading of paclitaxel for breast cancer therapy. Nat Commun. 2020;11:972.
28. Shigdar S, Agnello L, Fedele M, Camorani S, Cerchia L. Profiling Cancer Cells by Cell-SELEX: Use of Aptamers for Discovery of Actionable Biomarkers and Therapeutic Applications Thereof. Pharmaceutics. 2021;14:28.
29. Camorani S, Crescenzi E, Fedele M, Cerchia L. Oligonucleotide aptamers against tyrosine kinase receptors: Prospect for anticancer applications. Biochim Biophys Acta Rev Cancer. 2018;1869:263–77.
30. Camorani S, Hill BS, Fontanella R, Greco A, Gramanzini M, Auletta L, et al. Inhibition of Bone Marrow-Derived Mesenchymal Stem Cells Homing Towards Triple-Negative Breast Cancer Microenvironment Using an Anti-PDGFRβ Aptamer. Theranostics. 2017;7:3595–607.
31. Chen X, Song E. Turning foes to friends: targeting cancer-associated fibroblasts. Nat Rev Drug Discov. 2019;18:99–115.
32. Mao X, Xu J, Wang W, Liang C, Hua J, Liu J, et al. Crosstalk between cancer-associated fibroblasts and immune cells in the tumor microenvironment: new findings and future perspectives. Mol Cancer. 2021;20:131.
33. Plate KH, Breier G, Farrell CL, Risau W. Platelet-derived growth factor receptor-beta is induced during tumor development and upregulated during tumor progression in endothelial cells in human gliomas. Lab Invest. 1992;67:529–34.
34. Daynes RA, Dowell T, Araneo BA. Platelet-derived growth factor is a potent biologic response modifier of T cells. J Exp Med. 1991;174:1323–33.
35. Camorani S, Passariello M, Agnello L, Esposito S, Collina F, Cantile M, et al. Aptamer targeted therapy potentiates immune checkpoint blockade in triple-negative breast cancer. J Exp Clin Cancer Res. 2020;39:180.
36. Heldin CH, Westermark B. Mechanism of action and in vivo role of platelet-derived growth factor. Physiol Rev. 1999;79:1283–316.

37. Inaba T, Shimano H, Gotoda T, Harada K, Shimada M, Ohsuga J, et al. Expression of platelet-derived growth factor beta receptor on human monocyte-derived macrophages and effects of platelet-derived growth factor BB dimer on the cellular function. J Biol Chem. 1993;268:24353–60.
38. Fuhrman B, Gantman A, Khateeb J, Volkova N, Horke S, Kiyan J, et al. Urokinase activates macrophage PON2 gene transcription via the PI3K/ROS/MEK/SREBP-2 signalling cascade mediated by the PDGFR-beta. Cardiovasc Res. 2009;84:145–54.
39. Camorani S, Hill BS, Collina F, Gargiulo S, Napolitano M, Cantile M, et al. Targeted imaging and inhibition of triple-negative breast cancer metastases by a PDGFRβ aptamer. Theranostics. 2018;8:5178–99.
40. Monaco I, Camorani S, Colecchia D, Locatelli E, Calandro P, Oudin A, et al. Aptamer Functionalization of Nanosystems for Glioblastoma Targeting through the Blood-Brain Barrier. J Med Chem. 2017;60:4510–6.
41. Ricciardi L, Mastropietro TF, Ghedini M, La Deda M, Szerb EI. Ionic-pair effect on the phosphorescence of ionic iridium(III) complexes. J Organomet Chem. 2014;772–773:307–13.
42. Ricciardi L, Martini M, Tillement O, Sancey L, Perriat P, Ghedini M, et al. Multifunctional material based on ionic transition metal complexes and gold–silica nanoparticles: Synthesis and photophysical characterization for application in imaging and therapy. J Photochem Photobiol B. 2014;140:396–404.
43. Camorani S, Crescenzi E, Colecchia D, Carpentieri A, Amoresano A, Fedele M, et al. Aptamer targeting EGFRvIII mutant hampers its constitutive autophosphorylation and affects migration, invasion and proliferation of glioblastoma cells. Oncotarget. 2015;6:37570–87.
44. Camorani S, Granata I, Collina F, Leonetti F, Cantile M, Botti G, et al. Novel Aptamers Selected on Living Cells for Specific Recognition of Triple-Negative Breast Cancer. iScience. 2020;23:100979.
45. Mazzucchelli S, Piccotti F, Allevi R, Truffi M, Sorrentino L, Russo L, et al. Establishment and Morphological Characterization of Patient-Derived Organoids from Breast Cancer. Biol Proced Online. 2019;21:12.
46. Malik MA, Wani MY, Hashim MA. Microemulsion method: A novel route to synthesize organic and inorganic nanomaterials. Arab J Chem. 2012;5:397–417.
47. Han L, Terasaki O, Che S. Carboxylic group functionalized ordered mesoporous silicas. J Mater Chem. 2011;21:11033.
48. Kurtz-Chalot A, Klein JP, Pourchez J, Boudard D, Bin V, Alcantara GB, et al. Adsorption at cell surface and cellular uptake of silica nanoparticles with different surface chemical functionalizations: impact on cytotoxicity. J Nanopart Res. 2014;16:2738.
49. Amendola V, Pilot R, Frasconi M, Maragò OM, Iatì MA. Surface plasmon resonance in gold nanoparticles: a review. J Phys: Condens Matter. 2017;29:203002.
50. Entradas T, Waldron S, Volk M. The detection sensitivity of commonly used singlet oxygen probes in aqueous environments. J Photochem Photobiol B. 2020;204:111787.
51. Jauffred L, Samadi A, Klingberg H, Bendix PM, Oddershede LB. Plasmonic Heating of Nanostructures. Chem Rev. 2019;119:8087–130.

52. Odeh F, Nsairat H, Alshaer W, Ismail MA, Esawi E, Qaqish B, et al. Aptamers Chemistry: Chemical Modifications and Conjugation Strategies. Molecules. 2019;25:3.
53. Yüce M, Kurt H. How to make nanobiosensors: surface modification and characterisation of nanomaterials for biosensing applications. RSC Adv. 2017;7:49386–403.
54. Mutas M, Strelow C, Kipp T, Mews A. Specific binding and internalization: an investigation of fluorescent aptamer-gold nanoclusters and cells with fluorescence lifetime imaging microscopy. Nanoscale. 2018;10:20453–61.
55. Periasamy R, Elshaer SL, Gangaraju R. CD140b (PDGFRβ) signaling in adipose-derived stem cells mediates angiogenic behavior of retinal endothelial cells. Regen Eng Transl Med. 2019;5:1–9.
56. Avnet S, Lemma S, Cortini M, Di Pompo G, Perut F, Baldini N. Pre-clinical Models for Studying the Interaction Between Mesenchymal Stromal Cells and Cancer Cells and the Induction of Stemness. Front Oncol. 2019;9:305.
57. Ishiguro T, Ohata H, Sato A, Yamawaki K, Enomoto T, Okamoto K. Tumor-derived spheroids: Relevance to cancer stem cells and clinical applications. Cancer Sci. 2017;108:283–9.
58. Tchoryk A, Taresco V, Argent RH, Ashford M, Gellert PR, Stolnik S, et al. Penetration and Uptake of Nanoparticles in 3D Tumor Spheroids. Bioconjug Chem. 2019;30:1371–84.
59. Gencoglu MF, Barney LE, Hall CL, Brooks EA, Schwartz AD, Corbett DC, et al. Comparative Study of Multicellular Tumor Spheroid Formation Methods and Implications for Drug Screening. ACS Biomater Sci Eng. 2018;4:410–20.
60. Sarnella A, Ferrara Y, Albanese S, Omodei D, Cerchia L, De Simone G, et al. Inhibition of Bone Marrow-Mesenchymal Stem Cell-Induced Carbonic Anhydrase IX Potentiates Chemotherapy Efficacy in Triple-Negative Breast Cancer Cells. Cells. 2023;12:298.
61. Deynoux M, Sunter N, Ducrocq E, Dakik H, Guibon R, Burlaud-Gaillard J, et al. A comparative study of the capacity of mesenchymal stromal cell lines to form spheroids. PLoS ONE. 2020;15:e0225485.
62. Cesarz Z, Tamama K. Spheroid Culture of Mesenchymal Stem Cells. Stem Cells Int. 2016;2016:9176357.
63. McKenna MK, Ozcan A, Brenner D, Watanabe N, Legendre M, Thomas DG, et al. Novel banana lectin CAR-T cells to target pancreatic tumors and tumor-associated stroma. J Immunother Cancer. 2023;11:e005891.
64. Agnello L, d'Argenio A, Nilo R, Fedele M, Camorani S, Cerchia L. Aptamer-Based Strategies to Boost Immunotherapy in TNBC. Cancers (Basel). 2023;15:2010.
65. Chen F, Zeng Y, Qi X, Chen Y, Ge Z, Jiang Z, et al. Targeted salinomycin delivery with EGFR and CD133 aptamers based dual-ligand lipid-polymer nanoparticles to both osteosarcoma cells and cancer stem cells. Nanomedicine. 2018;14:2115–27.
66. Chen J, Li J, Sun X, Lu H, Liu K, Li Z, et al. Precision Therapy of Recurrent Breast Cancer through Targeting Different Malignant Tumor Cells with a HER2/CD44-Targeted Hydrogel Nanobot. Small. 2023;19:e2301043.

67. Kim M, Lee JS, Kim W, Lee JH, Jun BH, Kim KS, et al. Aptamer-conjugated nano-liposome for immunogenic chemotherapy with reversal of immunosuppression. J Control Release. 2022;348:893–910.
68. Jiang J, Chen H, Yu C, Zhang Y, Chen M, Tian S, et al. The promotion of salinomycin delivery to hepatocellular carcinoma cells through EGFR and CD133 aptamers conjugation by PLGA nanoparticles. Nanomed (Lond). 2015;10:1863–79.
69. Song L, Wang Z, Liu J, Wang T, Jiang Q, Ding B. Tumor-Targeted DNA Bipyramid for in Vivo Dual-Modality Imaging. ACS Appl Bio Mater. 2020;3:2854–60.
70. Liu X, Zhang G, Yu T, Liu J, Chai X, Yin D, et al. CL4-modified exosomes deliver lncRNA DARS-AS1 siRNA to suppress triple-negative breast cancer progression and attenuate doxorubicin resistance by inhibiting autophagy. Int J Biol Macromol. 2023;250:126147.
71. Xiao D, Huang Y, Huang S, Zhuang J, Chen P, Wang Y, et al. Targeted delivery of cancer drug paclitaxel to chordomas tumor cells via an RNA nanoparticle harboring an EGFR aptamer. Colloids Surf B Biointerfaces. 2022;212:112366.
72. Agnello L, d'Argenio A, Caliendo A, Nilo R, Zannetti A, Fedele M, et al. Tissue Inhibitor of Metalloproteinases-1 Overexpression Mediates Chemoresistance in Triple-Negative Breast Cancer Cells. Cells. 2023;12:1809.
73. Kim Y, Kim E, Wu Q, Guryanova O, Hitomi M, Lathia JD, et al. Platelet-derived growth factor receptors differentially inform intertumoral and intratumoral heterogeneity. Genes Dev. 2012;26:1247–62.
74. Huaijun F, Yang J, Nan J, Yuhan Z, Ningcheng W, Yifan L et al. Gint4.T-siHDGF chimera-capped mesoporous silica nanoparticles encapsulating temozolomide for synergistic glioblastoma therapy. Biomaterials. 2024;122479.
75. Shi S, Fu W, Lin S, Tian T, Li S, Shao X, et al. Targeted and effective glioblastoma therapy via aptamer-modified tetrahedral framework nucleic acid-paclitaxel nanoconjugates that can pass the blood brain barrier. Nanomedicine. 2019;21:102061.
76. Wang F, Zhou Y, Cheng S, Lou J, Zhang X, He Q, et al. Gint4.T-Modified DNA Tetrahedrons Loaded with Doxorubicin Inhibits Glioma Cell Proliferation by Targeting PDGFRβ. Nanoscale Res Lett. 2020;15:150.

Figures

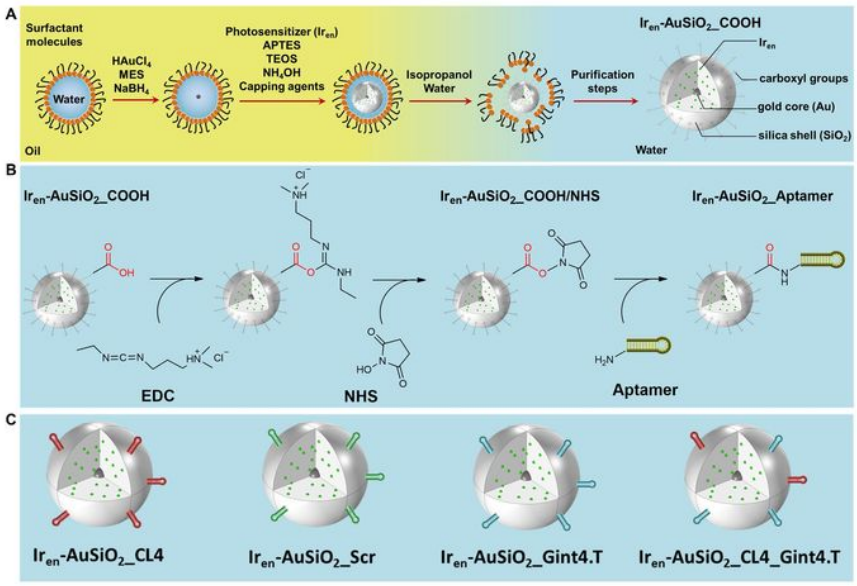

Figure 1

Figure 1

Schematic illustration of the protocol for the obtainment of the final nanoplatforms. **A** Ir_{en}-$AuSiO_2$_COOH preparation by reverse microemulsion technique. Surfactant: 4-(1,1,3,3-Tetramethylbutyl)phenyl-polyethylene glycol; Mesna: sodium 2-mercaptoethanesulfonate; APTES: (3-aminopropyl)triethoxysilane; TEOS: tetraethoxysilane; capping agents: 11-Triethoxysilylundecanoic acid and N-(3-triethoxysilyl) propylsuccinic anhydride. **B** Covalent crosslinking strategy to achieve aptamers-nanoplatforms conjugates

(Ir_{en}-$AuSiO_2$_Aptamer). EDC: N-(3-dimethylaminopropyl)-N'-ethylcarbodiimide hydrochloride; NHS: N-Hydroxysuccinimide. **C** Ir_{en}-$AuSiO_2$_Aptamer samples prepared and tested in this study.

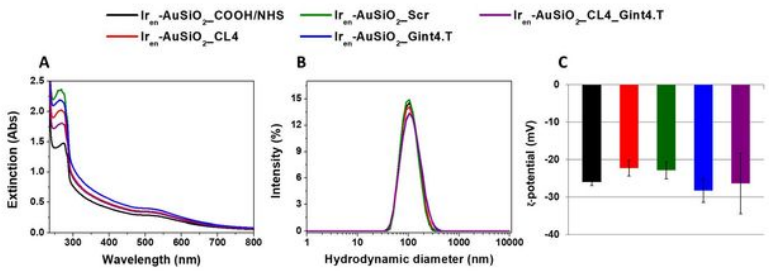

Figure 2

Figure 2

Characterization of Ir_{en}-$AuSiO_2$_Aptamer nanoplatforms. **A** UV-Vis spectra, **B** hydrodynamic diameters, **C** ζ-potential values of Ir_{en}-$AuSiO_2$_Aptamer nanoplatforms dispersed in water.

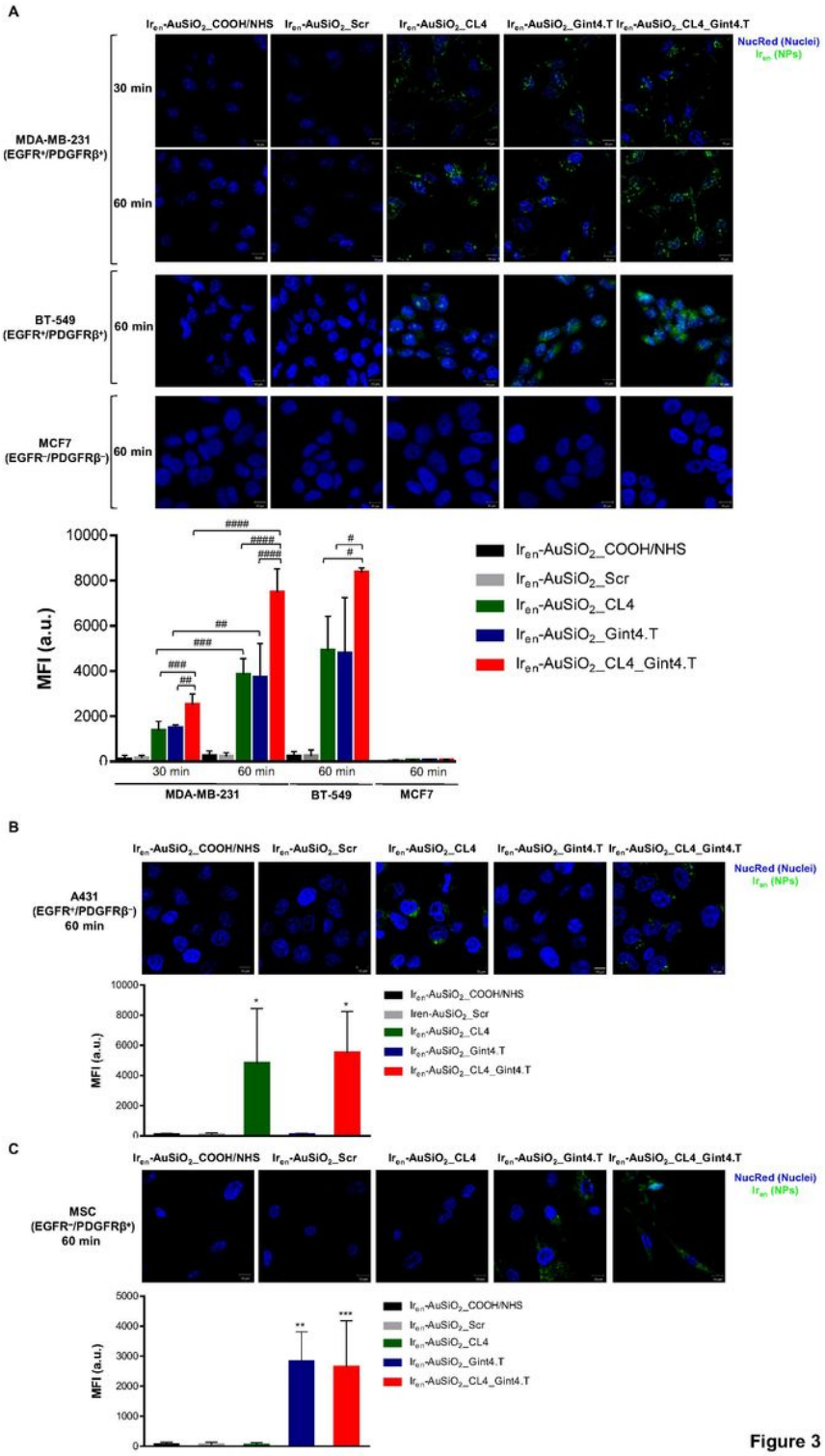

Figure 3

Figure 3

Selective cell uptake of CL4 and/or Gint4.T-decorated Ir$_{en}$-AuSiO$_2$_Aptamer nanoplatforms in 2D cultures. Representative confocal images of **A** MDA-MB-231 and BT-549 (EGFR$^+$/PDGFRβ$^+$), and MCF7 (EGFR$^-$/PDGFRβ$^-$) cells, **B** A431 (EGFR$^+$/PDGFRβ$^-$) cells, and **C** MSCs (EGFR$^-$/PDGFRβ$^+$) cells, incubated with Ir$_{en}$-AuSiO$_2$_Aptamer or unconjugated Ir$_{en}$-AuSiO$_2$_COOH/NHS nanoparticles at 37°C for the indicated times. After washing and fixation, cells were labeled with NucRed (blue) to stain nuclei, and nanoparticles are

displayed in green. Magnification: 63×, 1.0× digital zoom, scale bar = 10 µm. All digital images were captured under the same settings to enable a direct comparison of staining patterns. **A-C** Mean fluorescence intensity (MFI) was quantified using Zeiss software on at least ten separate images for each condition. Bars depict means ± SD (n = 3). *p<0.05, **p<0.01, ***p<0.001 relative to Ir_{en}-$AuSiO_2$_Scr; #p<0.05, ##p<0.01, ###p<0.001, ####p<0.0001.

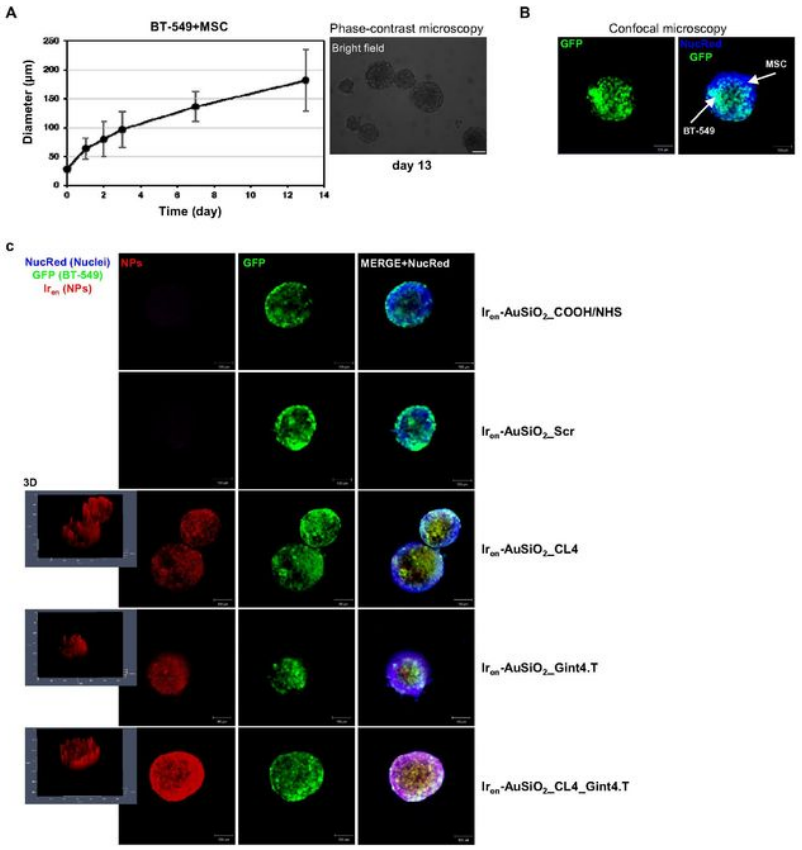

Figure 4

Figure 4

Selective uptake of CL4 and/or Gint4.T-decorated Ir_{en}-$AuSiO_2$_Aptamer nanoplatforms in 3D heterotypic spheroids. **A** (left) Growth kinetic of BT-549-GFP+MSC spheroids represented in spheroid diameter over 13 days. The representative phase-contrast microscopy images of spheroids formation over the course of seven days are reported in Supplementary Figure 7. Data are presented as the mean ± SD (n=3); (right) representative phase-contrast microscopy image of the spheroids grown at day 13. Magnification: 10×, scale bar = 100 µm. **B** Representative confocal image of the heterotypic spheroid at day 13. BT-549-GFP cells are visualized in green and nuclei, stained with NucRed 647, in blue. White arrows in the merged images highlight the mixed composition of the spheroid (MSC, blue; BT-549-GFP, blue light). **C** Representative confocal images of BT-549-GFP/MSC spheroids grown at day 13 and then incubated with Ir_{en}-$AuSiO_2$_CL4, Ir_{en}-$AuSiO_2$_Gint4.T, Ir_{en}-$AuSiO_2$_CL4_Gint4.T, Ir_{en}-$AuSiO_2$_Scr or unconjugated Ir_{en}-$AuSiO_2$_COOH/NHS for 24 h at 37°C. Nanoparticles, BT-549-GFP cells and nuclei are displayed in red, green and blue, respectively. 3D images are shown. **B**,**C** Magnification: 10×, 1.0× digital zoom, scale bar = 100 µm. All digital images were captured under the same settings to enable a direct comparison of staining patterns.

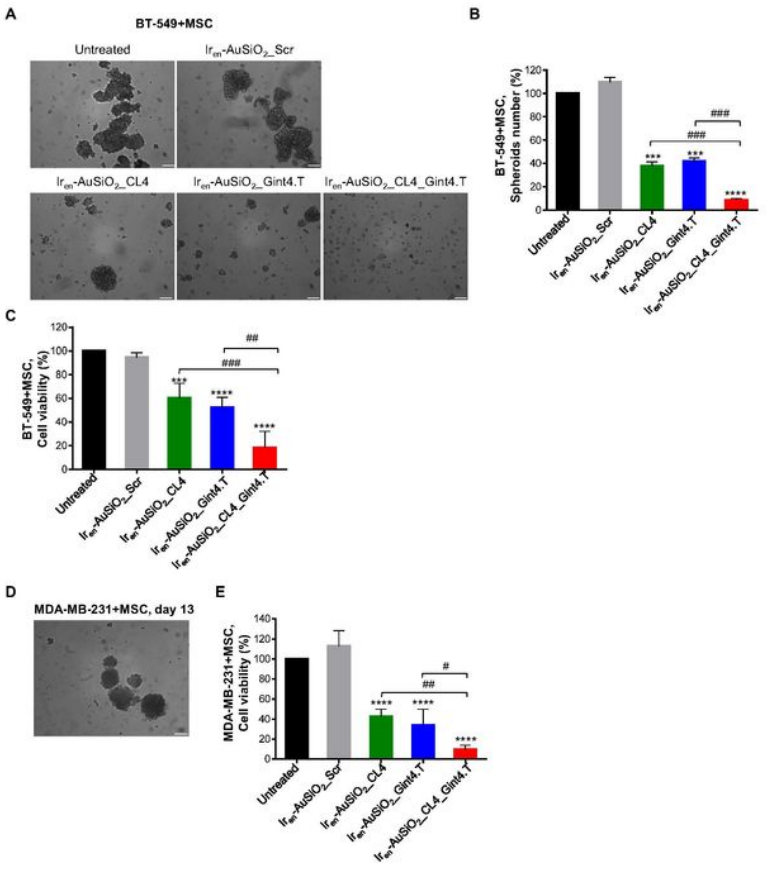

Figure 5

Figure 5

Anticancer activity of Ir$_{en}$-AuSiO$_2$_Aptamer nanoplatforms on 3D spheroids of EGFR$^+$/PDGFRβ$^+$ cancer cells and MSC. **A** (left) Representative phase-contrast microscopy images of BT-549/MSC spheroids treated with Ir$_{en}$-AuSiO$_2$_CL4, Ir$_{en}$-AuSiO$_2$_Gint4.T, Ir$_{en}$-AuSiO$_2$_CL4_Gint4.T or untargeted Ir$_{en}$-AuSiO$_2$_Scr. Spheroids treatment with specific aptamer-decorated nanoplatforms, but not with Ir$_{en}$-AuSiO$_2$_Scr, inhibits both the **B** number of spheroids and **C** cell viability, expressed as percentage of viable treated cells with respect to

untreated spheroids. **D** Representative phase-contrast microscopy image of MDA-MB-231/MSC spheroids grown at day 13. **E** Cell viability assay on MDA-MB-231/MSC spheroids treated as in A. **A**,**D** Magnification: 10×, scale bar = 100 µm. **B**,**C**,**E** Bars depict mean ± SD (n = 3). ***p<0.001, ****p<0.0001 relative to Ir_{en}-$AuSiO_2$_Scr; #p<0.05, ##p<0.01, ###p<0.001. No statistically significant variations among Ir_{en}-$AuSiO_2$_Scr and untreated were obtained.

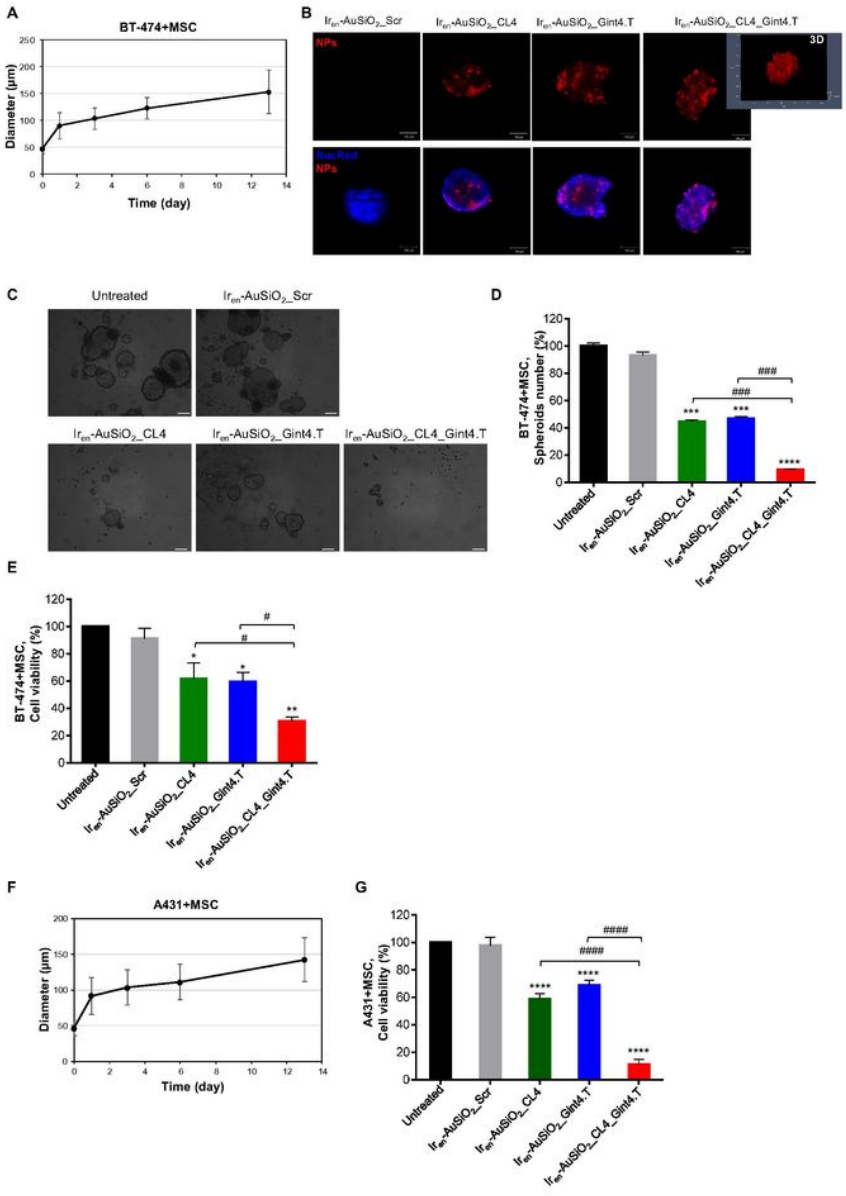

Figure 6

Figure 6

Anticancer activity of Ir_{en}-$AuSiO_2$_Aptamer nanoplatforms on 3D spheroids of $EGFR^+/PDGFR\beta^-$ cancer cells and MSC. **A** Growth kinetic of BT-474+MSC spheroids represented in spheroid diameter over 13 days. The representative phase-contrast microscopy images of spheroids formation over the course of thirteen days are reported in Supplementary Figure 9. **B** Representative confocal images of BT-474/MSC spheroids grown at day 13 and then incubated with Ir_{en}-$AuSiO_2$_CL4, Ir_{en}-$AuSiO_2$_Gint4.T, Ir_{en}-$AuSiO_2$_CL4_Gint4.T, or untargeted Ir_{en}-$AuSiO_2$_Scr for 24 h at 37°C. Nanoparticles and nuclei are displayed in red and blue, respectively. 3D image (Ir_{en}-$AuSiO_2$_CL4_Gint4.T) is shown. Magnification: 10×, 1.0× digital zoom, scale bar = 100 μm. All digital images were captured under the same settings to enable a direct comparison of staining patterns. **C** Representative phase-contrast microscopy images of BT-474/MSC spheroids treated as indicated. Spheroids treatment with specific aptamer-decorated nanoplatforms, but not with Ir_{en}-$AuSiO_2$_Scr, inhibits both the **D** number of spheroids and **E** cell viability, expressed as percentage of viable treated cells with respect to untreated spheroids. **F** Growth kinetic of A431+MSC spheroids represented in spheroid diameter over 13 days. The representative phase-contrast microscopy images of spheroids formation over the course thirteen days are reported in Supplementary Figure 9. **G** Cell viability assay on A431+MSC spheroids treated as in C. **A**,**D**,**E**,**F**,**G** Data are presented as the mean ± SD (n=3); *p<0.05, **p<0.01, ***p<0.001, ****p<0.001 relative to Ir_{en}-$AuSiO_2$_Scr; #p<0.05, ###p<0.001, ####p<0.0001. No statistically significant variations among Ir_{en}-$AuSiO_2$_Scr and untreated were obtained.

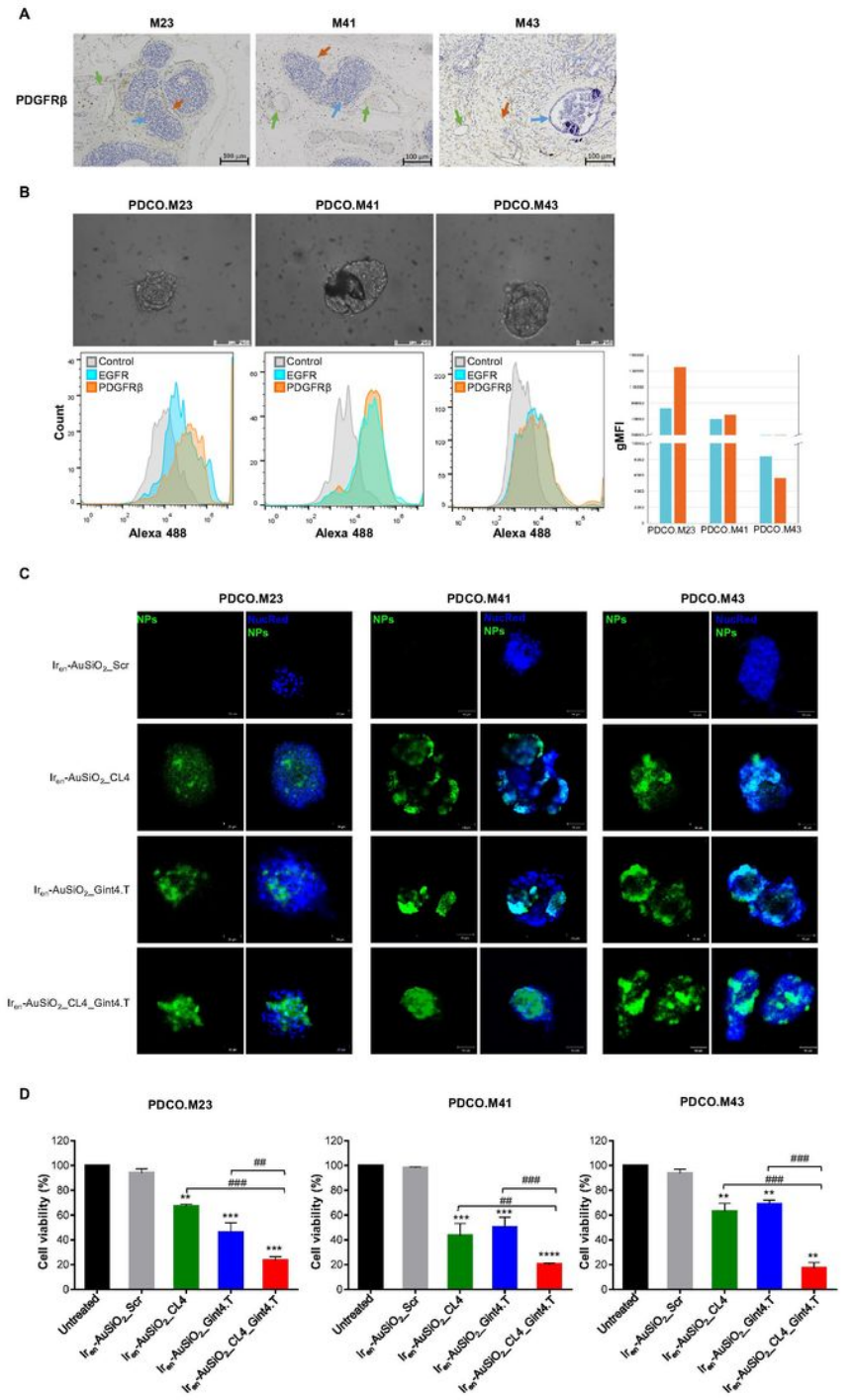

Figure 7

Figure 7

Anticancer activity of Ir$_{en}$-AuSiO$_2$_Aptamer nanoplatforms on 3D patient-derived breast cancer organoids. **A** Representative images of three breast cancer samples (M23, M41 and M43) stained by PDGFRβ. Magnification: 10×, scale bar = 100 μm. The blue arrows indicate negative neoplastic cells; the orange arrows indicate PDGFRβ-positive peritumoral stromal cells (M23 and M41, mild cytoplasmic expression; M43, moderate cytoplasmic expression); the green arrows indicate the endothelial cells of a vessel (red blood cells are visible inside) positive for PDGFRβ. **B** (upper) Representative phase-contrast microscopy

images of PDCOs obtained by M23, M41 and M43 tumor samples, magnification: 20×, scale bar = 250 μm; (lower) flow cytometry analyses to confirm the expression of EGFR and PDGFRβ in the three PDCOs. The histogram indicates the geometric mean fluorescence intensity (gMFI) of EGFR and PDGFRβ expressed on PDCOs, calculated using FlowJo software. **C** Representative confocal images of PDCO.M23, PDCO.M41 and PDCO.M43 incubated with Ir_{en}-$AuSiO_2$_CL4, Ir_{en}-$AuSiO_2$_Gint4.T, Ir_{en}-$AuSiO_2$_CL4_Gint4.T or untargeted Ir_{en}-$AuSiO_2$_Scr for 24 h at 37°C. Nanoparticles and nuclei are displayed in green and blue, respectively. Magnification: 10×, 2.0× digital zoom, scale bar = 50 μm. All digital images were captured under the same settings to enable a direct comparison of staining patterns. **D** Cell viability assay on PDCO.M23, PDCO.M41 and PDCO.M43 treated as indicated. Bars depict mean ± SD of two independent experiments performed in triplicate. **p<0.01, ***p<0.001, ****p<0.001 relative to Ir_{en}-$AuSiO_2$_Scr; ##p<0.01, ###p<0.001, ####p<0.0001. No statistically significant variations among Ir_{en}-$AuSiO_2$_Scr and untreated were obtained.

Supplementary Files

This is a list of supplementary files associated with this preprint. Click to download.

- SupplementaryInformation.pdf